

UC Davis

UC Davis Previously Published Works

Title

Influence of Agricultural Managed Aquifer Recharge and Stratigraphic Heterogeneities on Nitrate Reduction in the Deep Subsurface

Permalink

<https://escholarship.org/uc/item/8xf4m6md>

Authors

Waterhouse, Hannah
Arora, Bhavna
Spycher, Nicolas
et al.

Publication Date

2020-12-02

DOI

10.1002/essoar.10505069.1

Peer reviewed

27 **Abstract**

28 Agricultural managed aquifer recharge (AgMAR) is a proposed management strategy
29 whereby surface water flows are used to intentionally flood croplands with the purpose of
30 recharging underlying aquifers. However, legacy nitrate (NO_3^-) contamination in agriculturally-
31 intensive regions poses a threat to groundwater resources under AgMAR. To address these
32 concerns, we use a reactive transport modeling framework to better understand the effects of
33 AgMAR management strategies (i.e., by varying the frequency, duration between flooding
34 events, and amount of water) on N leaching to groundwater under different stratigraphic
35 configurations and antecedent moisture conditions. In particular, we examine the potential of
36 denitrification and nitrogen retention in deep vadose zone sediments using variable AgMAR
37 application rates on two-dimensional representations of differently textured soils, soils with
38 discontinuous bands/channels, and soils with preferential flow paths characteristic of typical
39 agricultural field sites. Our results indicate that finer textured sediments, such as silt loams, alone
40 or embedded within high flow regions, are important reducing zones providing conditions
41 needed for denitrification. Simulation results further suggest that applying recharge water all-at-
42 once, rather than in increments, increases denitrification within the vadose zone, but transports
43 higher concentrations of NO_3^- deeper into the profile. This transport into deeper depths can be
44 aggravated by wetter antecedent soil moisture conditions. We conclude that ideal AgMAR
45 management strategies can be designed to enhance denitrification in the subsurface and reduce N
46 leaching to groundwater, while specifically accounting for lithologic heterogeneity, antecedent
47 soil moisture conditions, and depth to the water table.

48
49 *Keywords:* Nitrate, Agricultural Management, Groundwater Banking, Spatial variability,
50 Managed Aquifer Recharge

51

52 **1. Introduction**

53 Nitrate (NO_3^-) contamination of freshwater resources from agricultural regions is an
54 environmental and human health concern worldwide (Rodell et al. 2018). In agriculturally
55 intensive regions, it is imperative to understand how management practices can enhance or
56 mitigate the effect of nitrogen loading to freshwater systems. In California, managed aquifer
57 recharge on agricultural lands is a proposed management strategy to counterbalance
58 unsustainable groundwater pumping practices. Agricultural managed aquifer recharge (AgMAR)
59 is an approach in which legally and hydrologically available surface water flows are captured
60 and used to intentionally flood croplands with the purpose of recharging underlying aquifers
61 (Kocis and Dahlke, 2017). AgMAR represents a shift away from the normal hydrologic regime
62 wherein high efficiency irrigation application occurs mainly during the growing season. In
63 contrast, AgMAR involves applying large amounts of water over a short period during the winter
64 months. This change in winter application rates has the potential to affect the redox status of the
65 unsaturated (vadose) zone of agricultural regions with implications for nitrogen (N) fate and
66 transport to freshwater resources.

67 Most modeling studies targeting agricultural N contamination of groundwater are limited
68 to the root zone; these studies assume that once NO_3^- has leached below the root zone, it behaves
69 as a conservative tracer until it reaches the underlying groundwater (Harter et al. 2008, Botros et
70 al. 2012, van der Laan et al. 2013, Baram et al. 2016, Ascott et al. 2016 & 2017) or, these studies

71 employ first order decay coefficients to simplify N cycling reactions (Hanson et al. 2006, Phogat
72 et al. 2014, Salehi et al. 2017). However, recent laboratory and field-based investigations in
73 agricultural systems with deep unsaturated zones have shown the potential for N cycling, in
74 particular denitrification, well below the root zone (Xiang et al. 2008, Jahangir et al. 2012,
75 Peterson et al. 2013, Pratt et al. 1972). Moreover, in agricultural settings, especially in
76 alluvial basins such as in California with a history of agriculture, large amounts of legacy NO_3^-
77 has built up over years from fertilizer use inefficiencies and exists within the deep subsurface
78 (Van Meter et al. 2016, Waterhouse et al. 2020). It is not yet clear how this legacy nitrogen may
79 respond to changing hydrologic regimes and variations in AgMAR practices, and more
80 importantly, if flooding agricultural sites is enhancing nitrate transport to the groundwater or
81 attenuating it by supporting *in situ* denitrification.

82 Several studies have documented that denitrification rates in the deep subsurface vary as
83 a function of NO_3^- , carbon, and oxygen concentrations as well as other environmental factors
84 (e.g., pH, temperature, texture, iron) (Arora et al., 2013; Dwivedi et al., 2018; Yabusaki et al.,
85 2017). While total soil organic carbon typically declines with depth (Syswerda et al. 2011),
86 dissolved organic carbon (DOC) can be readily transported by water lost from the root zone to
87 deeper layers (Bundt et al. 2001, Jardine et al. 2006) and can therefore be available to act as an
88 electron donor for denitrification (Peterson et al. 2013, Cressey et al. 2018). Oxygen
89 concentration in the vadose zone is maintained by advective and diffusive transport, while
90 oxygen consumption occurs via microbial metabolic demand and/or abiotic chemical reactions
91 (Akhavan et al. 2013, Dutta et al. 2015). The effects of drying and wetting cycles on oxygen (O_2)
92 concentrations in the deep subsurface are not well documented, however, there is some evidence
93 that O_2 consumption proceeds rapidly as saturation increases and rebounds quickly during dry
94 periods (Dutta et al. 2015). These variations in oxygen concentration can influence N cycling
95 and, thus, transport to groundwater. Therefore, a gap currently exists in quantifying N
96 attenuation and transport from agriculturally intensive regions with a “deep” vadose zone while
97 accounting for the many competing N cycle reactions and transformations, as impacted by
98 different hydrological regimes imposed under AgMAR.

99 The application of AgMAR itself can vary in terms of the hydraulic loading and rates
100 used, as well as the duration between flood water applications. These can in turn affect water
101 retention times, O_2 availability, consumption of electron donors (carbon) and consequently
102 denitrification rates (Akhavan et al. 2013). For example, denitrification rates were found to
103 increase with increased hydraulic loading and with shorter times between flood applications
104 within the vadose zone of a rapid infiltration basin system used for disposing of treated
105 wastewater (Akhavan et al. 2013). In shallow, sandy soils, high flow rates - above an infiltration
106 threshold - were negatively correlated with denitrification rates, suggesting that an optimum
107 infiltration rate exists for a given sediment stratigraphy to maximize NO_3^- reduction (Schmidt et
108 al. 2011). Given the immense stratigraphic heterogeneity in alluvial basins, such as in
109 California’s Central Valley, a range of optimum infiltration rates may exist with implications for
110 managing AgMAR differently based on the geologic setting of the intended site. Therefore, the
111 objectives of this study are to: a) understand the effects of varying stratigraphy and hydrologic
112 regimes on denitrification rates, and b) identify AgMAR management scenarios that increase
113 denitrification rates, such that the potential for N leaching to groundwater is decreased.

114 Herein, we focus on an agricultural field site in Modesto, California located within the
115 Central Valley of California, which is responsible for California’s \$46 billion-dollar agricultural

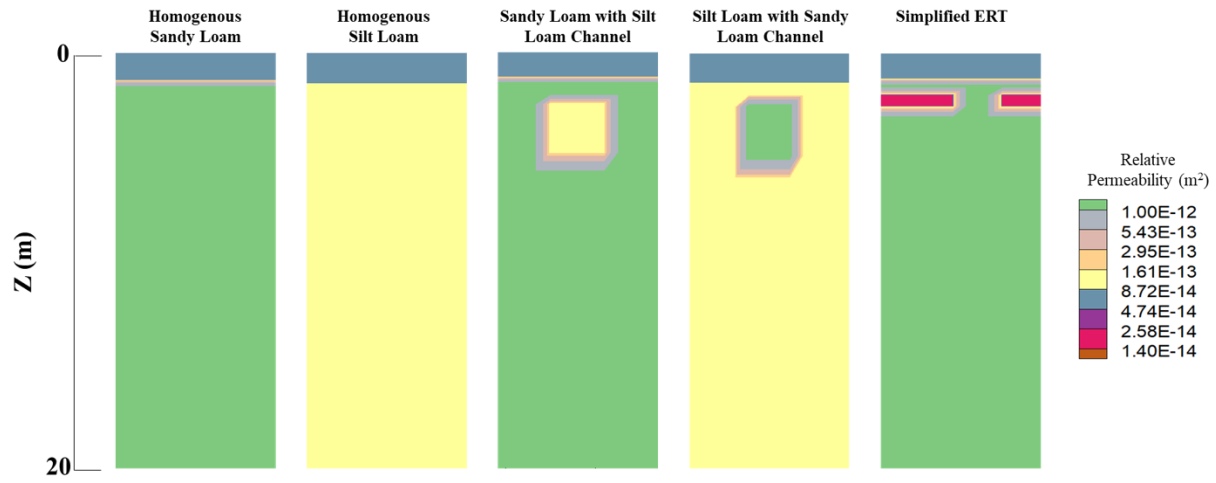
116 economy (CDFA, 2017). The field site typifies the deep vadose zones prevalent in this region,
117 which are characterized by heterogenous layered alluvial sediments intercalated with
118 discontinuous buried clay and carbon rich paleosols (Weissman et al. 2002a, 2002b, Bennet et al.
119 2006, Chaopricha and Marín-Spiotta, 2014, Marín-Spiotta et al. 2014). These banded features,
120 especially the paleosols, as well as areas of preferential flow, are typically associated with
121 enhanced biogeochemical activity, higher carbon content and availability of metabolic substrates
122 such as nitrogen (Brockman et al. 1992, Bundt et al. 2001). These regions respond to and change
123 depending on environmental conditions such as water content and oxygen concentration *in situ*
124 that are influenced by the hydrologic regime at the surface and may be important for NO_3^-
125 attenuation and reduction prior to reaching the water table. Therefore, this study considers
126 varying hydrologic regimes and stratigraphic variations (including preferential flow paths and
127 discontinuous bands/channels) that are prevalent in the region. More specifically, at the Modesto
128 field site (which is described in more detail below), large amounts of legacy N already reside in
129 the vadose zone, while N fertilizer application and irrigation occurs throughout the spring and
130 summer months. AgMAR, if implemented, occurs during the winter months as water becomes
131 available. Therefore, we focus here on quantifying the effects of AgMAR on N cycling in the
132 deep vadose zone and implications for NO_3^- contamination of groundwater at this characteristic
133 agricultural field site. We also investigate the specific AgMAR application rates that would
134 increase the effectiveness of *in situ* denitrification under different stratigraphic configurations
135 through the development and testing of a reactive transport model. We believe such an analysis
136 provides important insights for the successful application of AgMAR strategies aimed at
137 improving groundwater storage in a changing climate.

138

139 **2. Modeling Strategy**

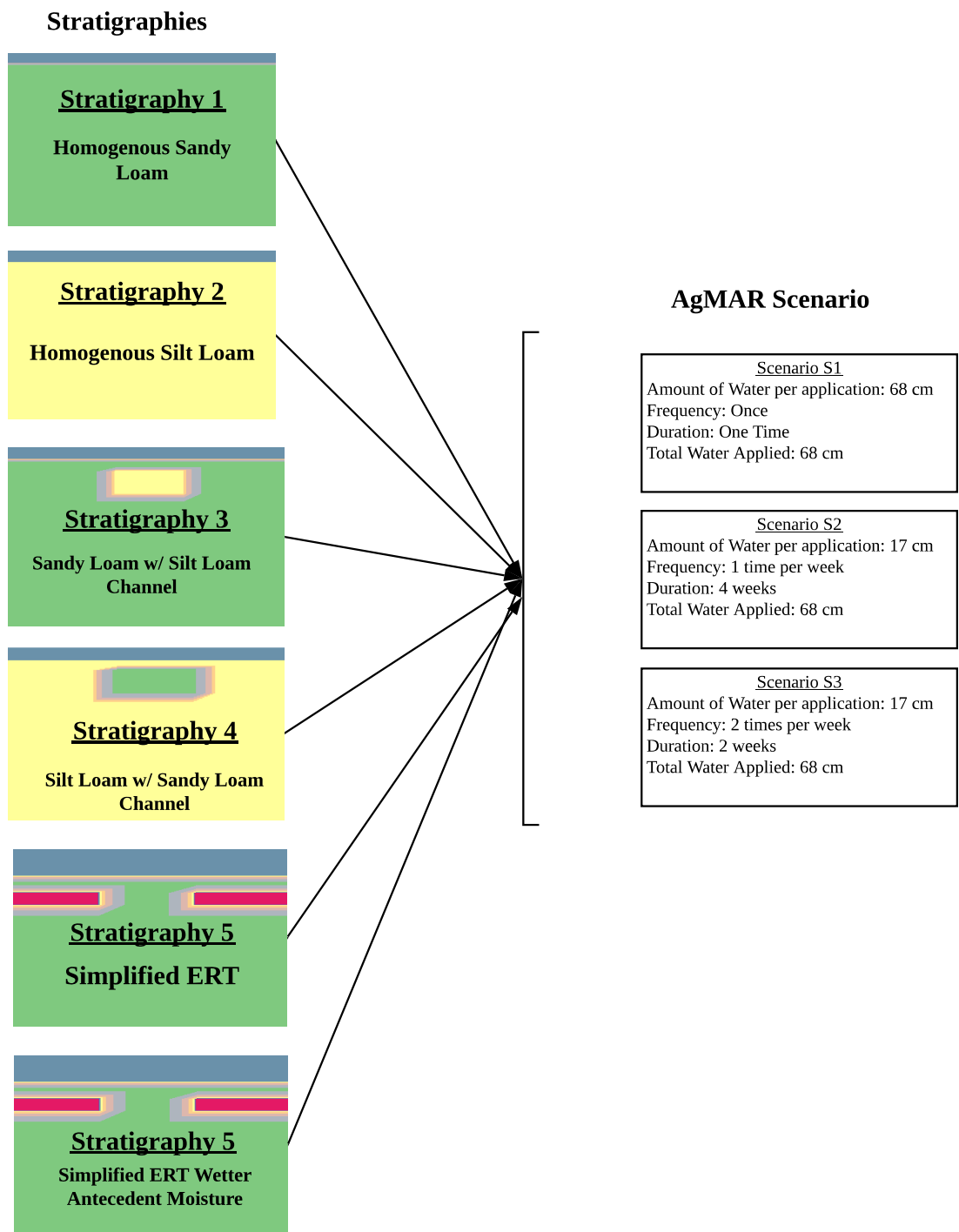
140 Reactive transport models can be beneficial tools to elucidating N fate and transport in
141 deep vadose zone environments. Herein, we develop a comprehensive reaction network
142 incorporating the major processes impacting N transport and attenuation, such as aqueous
143 complexation, mineral precipitation and dissolution, and microbially mediated redox reactions.
144 While using the same reaction network, we implement several numerical scenarios to quantify
145 the range of denitrification rates possible under different AgMAR implementation strategies and
146 stratigraphic configurations (Figure 1 & Figure 2). For the latter, we used four different
147 stratigraphic configurations with a low permeability layer on top including i) two homogeneous
148 textural profiles, ii) a sand stratigraphy with a discontinuous silt band, iii) a silt stratigraphy with
149 a discontinuous sand band, and iv) a complex stratigraphy more representative of the field
150 conditions investigated by electrical resistance tomography (ERT). The top layer was specifically
151 calibrated to match measured average field infiltration rates of 0.17 cm/hr. For each stratigraphy,
152 we further varied the frequency and duration of water per application to investigate the impact of
153 different AgMAR implementations that are similar to recent field trials conducted throughout the
154 state (Bachand et al. 2014). In addition, we tested the effect of antecedent moisture conditions on
155 N biogeochemistry within the more complex stratigraphy by setting the model with a wetter
156 initial moisture profile. Overall, a set of 18 simulation experiments were used to isolate and
157 understand the contribution of different AgMAR strategies to enhance or decrease denitrification
158 rates in deep vadose zone environments with homogeneous and banded configurations. A
159 detailed model setup and numerical implementation is provided in Section 4.

160
161



162
163
164

Figure 1: Five varying stratigraphic profiles based on structural features from ERT profiles.



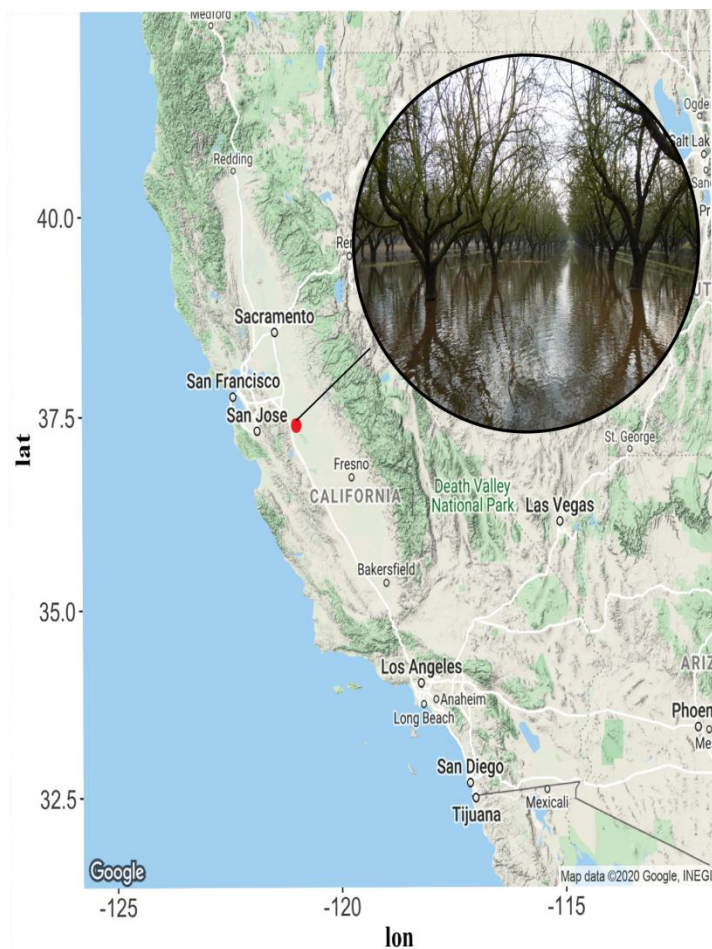
165
 166 **Figure 2: Conceptual diagram of modeling scenarios including the five stratigraphy**
 167 **scenarios overlain by each AgMAR management scenario (S1 to S3).**

168

169 **3. Field Site and Datasets**

170 **3.1. Study Site**

171 The study site is an almond orchard located in California’s Central Valley, southwest of
 172 Modesto, and north of the Tuolumne River (Figure 3). The surface soil is classified as a Dinuba
 173 fine sandy loam (coarse-loamy, mixed, active, thermic, Typic Haploxeralf). The site is
 174 characterized by a Mediterranean climate, with wet winters and hot, dry summers. Average
 175 annual temperature and total annual precipitation are 17.5° C and 335 mm, respectively. As
 176 suggested above, the vadose zone typifies the valley with contrasting layered sequences of
 177 granitic alluvial sedimentary deposits consisting of predominantly silt loams and sandy loams.
 178 We therefore use these textures to design our modeled stratigraphic configurations with and
 179 without banded layers. The groundwater table in the study area typically occurs around 15 m
 180 below ground surface. Soil properties including percent sand, silt, clay, total N, total C, and pH
 181 are shown in Table 1.
 182



183 **Figure 3: Map of study area in Modesto, CA with a picture of the actual field site during an**
 184 **AgMAR flooding event.**
 185

186

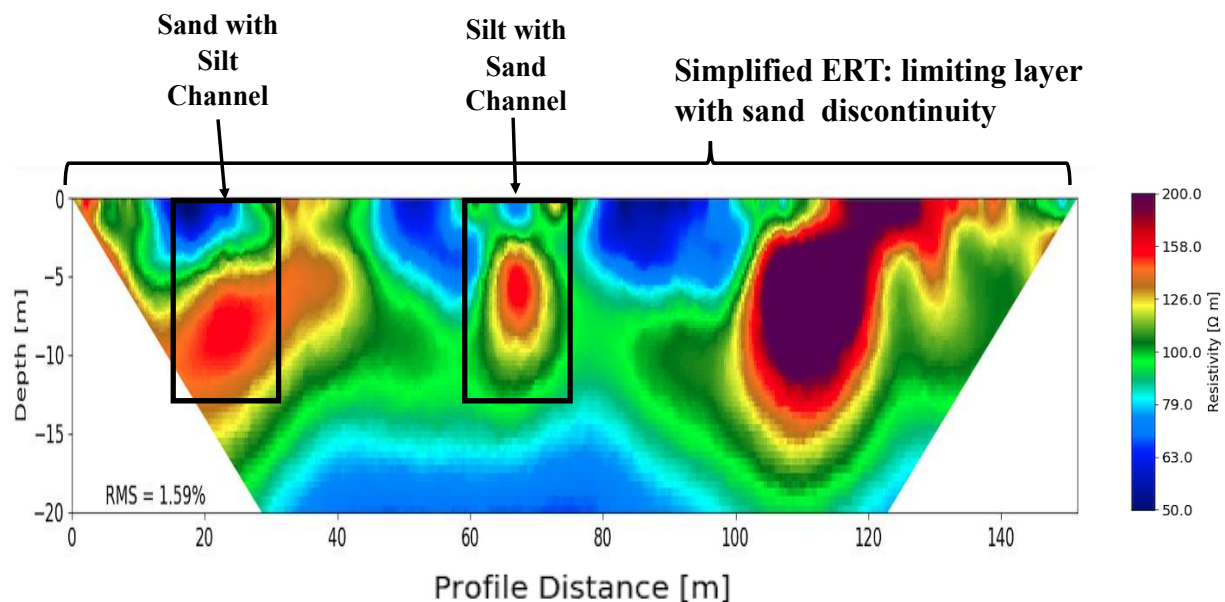
187 **Table 1: Soil properties averaged by depth (per meter) with standard errors in parentheses**
 188 **(n=5/meter).**

| Depth (cm) | Sand (%) | Silt (%) | Clay (%) | Total N (%) | Total C (%) | NO ₃ ⁻ -N (ug/g) | pH |
|---------------|--------------|--------------|--------------|----------------|----------------|---|-------------|
| 0-25 | 46.24 (7.68) | 46.13 (7.49) | 7.64 (0.72) | 0.048 (0.01) | 0.73 (0.11) | 10.19 (4.18) | 6.71 (0.15) |
| 100-200 | 42.41 (6.49) | 48.64 (5.53) | 8.95 (2.64) | 0.050 (0.03) | 0.21 (0.04) | 13.81 (4.63) | 6.99 (0.10) |
| 200-300 | 48.39 (9.57) | 43.19 (8.16) | 8.43 (2.57) | 0.050 (0.03) | 0.068 (0.02) | 5.09 (1.38) | 6.99 (0.09) |
| 300-400 | 56.09 (9.93) | 37.64 (8.36) | 6.27 (1.71) | 0.010 (0.01) | 0.048 (0.02) | 3.26 (1.07) | 6.99 (0.10) |
| 400-500 | 78.96 (8.13) | 18.12 (7.42) | 2.92 (0.78) | 0.004 (0.001) | 0.056 (.03) | 1.11 (0.34) | 6.92 0.07) |
| 500-600 | 55.60 (7.39) | 33.34 (5.54) | 11.06 (2.14) | 0.006 (0.001) | 0.065 (0.02) | 1.37 (0.31) | 7.07 (0.07) |
| 600-700 | 60.56 (8.05) | 35.38 (7.47) | 4.06 (1.21) | 0.060 (0.05) | 0.035 (0.02) | 0.57 (0.13) | 7.18 (0.07) |
| 700-800 | 75.45 (4.93) | 16.59 (3.63) | 7.96 (1.44) | 0.120 (0.07) | 0.027 (0.01) | 0.83 (0.17) | 7.26 (0.09) |
| 800-900 | 84.11 (4.27) | 10.56 (3.63) | 5.33 (1.35) | 0.020 (0.01) | 0.099 (0.02) | 1.71 (0.37) | 7.17 (0.11) |

189
190

191 **3.2. Characterization of the Deep Vadose Zone**

192 To specifically characterize the textural layers and subsurface heterogeneity at our site,
 193 we used electrical resistivity tomography (ERT) (Ulrich et al. 2020, in preparation). ERT profiles
 194 were generated along a 150 m transect to 20 m depth prior to flooding to quantify subsurface
 195 heterogeneity while the subsurface was relatively dry (Figure 4). Further, to validate the texture
 196 profiles generated by the ERT data, a set of six cores were taken along the transect of the ERT
 197 line down to nine meters with a Geoprobe push-drill system (Geoprobe Systems, Salina, KS).
 198 The first meter of the core was sampled every 25 cm. Thereafter, cores were sampled based on
 199 stratigraphy as determined by changes in color or texture. The ERT profiles were used to develop
 200 the stratigraphic modeling scenarios and the coring guided the specification of the hydraulic
 201 parameters. Redoximorphic features (i.e., changes in concentration and depletion of Fe) were
 202 noted throughout the cores.
 203



204

205 **Figure 4: Electrical resistivity tomography image of a 2D transect at our field site. More**
 206 **conductive layers are in blue and more resistive layers are in red.**

207

208 **3.3. Soil and Vadose Zone Physical and Chemical Analysis**

209 Texture was analyzed using a modified pipette method whereby 5 g of soil were placed in
 210 50 mL centrifuge tubes with 40 mL of 0.5% sodium phosphate and shaken overnight (Soil
 211 Survey Laboratory Methods Manual, 2004). Samples were hand shaken immediately before a 2.5
 212 mL aliquot was taken 11 seconds (sand fraction) and 1 hour and 51 minutes (clay fraction),
 213 respectively after shaking and placed in a pre-weighed tin. Tins were oven dried at 105°C
 214 overnight and reweighed the next day. Silt fractions were calculated by subtracting the sand and
 215 clay fraction from 1.

216 Nitrate (NO_3^-) and ammonium (NH_4^+) were analyzed by weighing 8-10 g of soil into a
 217 50-mL centrifuge tube and extracted with 2M KCl. Samples were centrifuged and the
 218 supernatant was analyzed colorimetrically for soil NO_3^- and NH_4^+ using a UV mini 1240,
 219 Shimadzu spectrophotometer as per methods described in Doane and Horwath (2003).
 220 Gravimetric water content was determined after soil samples were dried over night at 105° C.
 221 Total nitrogen (N) and soil organic carbon (SOC) were measured via combustion on a Costech
 222 ECS 4010 CHNSO elemental analyzer using soil samples that were dried at 60° C and
 223 pulverized using a ball mill. Samples were checked for carbonates using a 1 mol L⁻¹ hydrochloric
 224 acid (HCl) solution prior to combustion. A 1:1 water to soil ratio was placed in a falcon tube,
 225 shaken for an hour, allowed to settle, and the supernatant pH measured (Thomas, 1996).

226 Total reactive iron was measured by extracting 1 g of soil with 0.25 M hydroxylamine
 227 hydrochloride and 0.25 M HCl, shaking for 1 hour, and reacting with ferrozine (3-(2-pyridyl)-
 228 5,6-diphenyl-1,2,4-triazine-4',4''-disulfonate) and measured at 565 nm on a spectrophotometer
 229 (Lovley and Phillips 1987, Stookey 1970, Violler et al. 2000). Sulfur and manganese were
 230 determined on the supernatant of the same solution by the UC Davis ICPMS. Using a 1:4 ratio of
 231 soil to 0.5 M K_2SO_4 , dissolved organic carbon (DOC) was extracted, shaken for 1 hour,

232 centrifuged for 10 min at 3000xg, and analyzed on a UV-persulfate total organic carbon analyzer
233 (Phoenix 8000, Tekmar Dohrmann™, Cincinnati, OH).
234

235 **3.4. Acetylene Inhibition Method for Measuring Denitrification Capacity for Model** 236 **Development**

237 Soil cores taken after the AgMAR event were used to carry out microcosm experiments
238 under anaerobic conditions in a helium atmosphere at 22°C to determine denitrification capacity
239 according to a modified method by Groffman et al. (1999) and detailed in Waterhouse et al.
240 (2020, in prep). The N₂O and CO₂ measurements after the third and final day of the incubation
241 were used to inform the reaction rate parameters for denitrification. In particular, we used the
242 Q₁₀ equation to adjust the reaction parameters. This is because the Q₁₀ equation can account for
243 the temperature sensitivity of the reaction by calculating the change in the rate of a reaction
244 given a 10 °C change in temperature (Kirschbaum, 1995). Given that our field site temperatures
245 were lower during the winter (mean of 18 °C) than the temperatures at which the denitrification
246 capacity assays were incubated, we estimated the reaction rate using the following equation
247 (Meyer et al. 2018):

$$248 \quad R_2 = R_1 \times Q_{10}^{(T_2 - T_1)/10} \quad [1]$$

249 where R₁ and R₂ are the reaction rates at two different temperatures, T₁ and T₂ (°C), respectively,
250 and Q₁₀ is the factor by which the reaction rate increases when the temperature is raised by ten
251 degrees.
252

253 **4. Description of the Modeling Framework**

254 **4.1. Statistical Analysis**

255 Exploratory data analysis was performed on all physical and geochemical measurements
256 collected on the soil cores to establish normality conditions (or lack thereof). Almost all
257 variables were found to be non-normally distributed based on the Kolmogorov-Smirnov test.
258 Therefore, we used only conservative, non-parametric statistics to analyze the complete dataset
259 involving variables like pH, N₂O, NO₃⁻, NH₄⁺, DOC, Fe, Mn, S, total C, percent sand, silt, and
260 clay, and depth. Variables were standardized using the median and mean absolute distance and a
261 Spearman's rank correlation was conducted on the dataset. Correlation analysis was used to
262 delineate the impact of spatial layering or textural heterogeneity on N concentrations, if any.
263 Correlations between variables with p-values less than 0.05 were considered to be significant. To
264 further understand how the data grouped, a cluster analysis was conducted using the partitioning
265 around medoids method. Interestingly, data were found to group according to textural classes
266 and depth, which provides a mechanism to formulate the modeling framework.

267 **4.2. Simulation Model**

268 We used the reactive transport code TOUGHREACT V3.32-OMP (Xu et al. 2017,
269 Sonnenthal et al. 2014) to quantify the fate and transport of nitrogen in the deep vadose zone of
270 our study site. For this study, the EOS3 module of TOUGHREACT was used to simulate
271 coupled isothermal, multiphase (water and air) flow and multicomponent reactive transport in the
272 vadose zone (Sonnenthal et al. 2014; Pruess et al. 1999).

273

274 **4.2.1. Model Setup and Scenarios**

275 Several scenarios were developed based on the soil textures identified in cores and the
276 ERT profiles to provide insights into the effect of stratigraphic heterogeneity and AgMAR
277 management strategies on NO_3^- cycling in the deep subsurface, as described in section 2 above.
278 The five stratigraphies modeled in this study are shown in Figure 1. The claypan in the ERT
279 scenario spans 187 cm to 234 cm based on field observations. For each lithologic profile, three
280 AgMAR management strategies were imposed at the top boundary between 20 m and 150 m of
281 each modeled profile (Figure 2). For each AgMAR management strategy, the same overall
282 amount of water was applied, but the frequency, duration between flooding events, and amount
283 of water applied in each flooding event varied (as shown in Figure 2): a total of 68 cm of water
284 was applied either all at once (scenario S1), in increments of 17 cm once a week for four weeks
285 (scenario S2), in increments of 17 cm twice a week for two weeks (scenario S3), and all three
286 scenarios with an initially wetter moisture profile (Figure 2). Note, that for all scenarios, the
287 same reactions were considered, the water table was maintained at 15 m, and temperature was
288 fixed across depths at 18°C, the mean air temperature for January to February in Modesto.

289 For all scenarios, the modeling domain consists of a two-dimensional 20-meter deep
290 vertical cross-section extending laterally 2,190 m and including a 190 m wide zone of interest
291 located at its center, thus distant from lateral boundaries on each side by 1,000 m to avoid
292 boundary effects. The zone of interest was discretized using a total of 532 grid blocks with a
293 uniform grid spacing of 1 m along the horizontal axis, and a grid spacing of 0.02 m in the
294 unsaturated zone increasing with depth to 1 m in the saturated zone. A maximum time step of 1
295 day was specified for all simulated scenarios, although the actual time step was limited by
296 specifying a Courant Number of 0.5, typically resulting in much smaller time steps during early
297 stages of flooding.

298 Before each flooding simulation, the model was run first to hydrologic steady state
299 conditions including the effect of average (background) rainfall (33 cm year⁻¹). The water table
300 was set at a depth of 15 m by specifying a constant pressure at the bottom model boundary ($1.5 \times$
301 10^5 Pa at a depth of 20 m), and the model side boundaries (1000 m away from the zone of
302 interest) were set to no-flow conditions.

303 Under these hydrologic conditions, the model was then run for a 100-yr time period
304 including biogeochemical reactions and fixed atmospheric conditions of O_2 and CO_2 partial
305 pressures at the top boundary, a period after which essentially steady biogeochemical conditions
306 were achieved, including the development of progressively reducing conditions with depth
307 representative of field conditions. For these simulations, the concentrations of dissolved species
308 in background precipitation and in groundwater at the bottom model boundary were fixed, with
309 compositions described in Table 2 to yield similar vertically distributed NO_3^- concentrations as
310 were measured in the soil cores.

311 Flooding scenarios were then started from the initially steady flow and biogeochemical
312 conditions developed as described above. For these simulations, a free surface boundary was
313 implemented for scenario S1 where 68 cm of water was applied all at once. In contrast, a
314 specified flux boundary condition was imposed for the scenarios S2-S3, where floodwater
315 applications were broken up over a week. The flood water composition is discussed in Section
316 4.4.

317
 318 **Table 2: Aqueous concentrations of primary species applied as fixed concentrations at the**
 319 **top of the model boundary and in the flood water. Concentrations are in mol L⁻¹, unless**
 320 **otherwise specified.**

| | Initial Water | Flood Water |
|------------------------------------|------------------------------|-----------------------------|
| pH^(a) | 7.5 | 8 ^b |
| O₂ (aq) | 2.0947 x 10 ⁻⁴ | 2.0947 x 10 ^{-4 c} |
| SiO₂ (aq) | 6.8266 x 10 ⁻⁴ | 6.8266 x 10 ⁻⁶ |
| Na⁺ | 1.8276 x 10 ⁻³ | 1.8276 x 10 ⁻⁵ |
| K⁺ | 7.4203 x 10 ⁻⁵ | 7.4203 x 10 ⁻⁷ |
| Ca²⁺ | 9.7350 x 10 ^{-4 d} | 9.7350 x 10 ⁻⁶ |
| Mg²⁺ | 3.4986 x 10 ⁻⁴ | 3.4986 x 10 ⁻⁶ |
| HCO₃⁻ | 4.0580 x 10 ^{-3 d} | 1.6545 x 10 ^{-5 e} |
| SO₄²⁻ | 1.2497x10 ⁻⁴ | 1.2497x10 ⁻⁶ |
| Cl⁻ | 6.7723 x 10 ⁻⁴ | 6.7723 x 10 ⁻⁴ |
| HS⁻ | 1.0000 x 10 ⁻²⁰ | 1.0000 x 10 ⁻²⁰ |
| NO₃⁻ | 7.1378 x 10 ⁻⁴ | 7.1378 x 10 ⁻⁶ |
| NO₂⁻ | 9.3504 x 10 ⁻⁷ | 9.3504 x 10 ⁻⁹ |
| N₂ | 1.0000 x 10 ⁻²⁰ | 1.0000 x 10 ⁻²⁰ |
| NH₃ (aq) | 1.0000 x 10 ⁻⁸ | 1.0000 x 10 ⁻⁹ |
| Al³⁺ | 6.6965 x 10 ^{-10 f} | 1.0000 x 10 ⁻²⁰ |
| Fe³⁺ | 1.1582 x 10 ^{-19 g} | 1.0000 x 10 ⁻²⁰ |
| Fe²⁺ | 8.3000 x 10 ⁻²⁰ | 8.3000 x 10 ⁻²⁰ |
| Ba²⁺ | 4.1524 x 10 ⁻⁷ | 1.0000 x 10 ⁻²⁰ |
| Sr²⁺ | 5.1722 x 10 ⁻⁶ | 1.0000 x 10 ⁻²⁰ |
| Acetate | 1.1895 x 10 ^{-5 h} | 1.1895 x 10 ^{-7 h} |

321 ^(a) pH units
 322 ^(b) adjusted for charge balance
 323 ^(c) Fixed by P_{O2} (g) of 10^{-0.7} bar
 324 ^(d) Fixed by equilibrium with calcite
 325 ^(e) Fixed by P_{CO2} (g) of 10^{-3.4} bar
 326 ^(f) Fixed by equilibrium with k-feldspar

327 ^(g) Fixed by equilibrium with ferrihydrite

328 ^(h) Fixed by equilibrium with cellulose

329

330 4.3. Hydrological and Transport Properties

331 The Rosetta pedotransfer function model (Schaap et al. 2001) was used to estimate van
 332 Genuchten-Mualem parameters for the dominant textural classes identified through cluster
 333 analyses (Section 5.1). The hydraulic properties of the top layer were adjusted to match the
 334 average infiltration rate of the field experiments of 0.17 cm/hr. Table 3 shows the van
 335 Genuchten-Mualem parameters used in this study. Relative permeability values were calculated
 336 from the saturated hydraulic conductivity.

337

338 **Table 3: Hydraulic parameters used in this study. $K_{s,z}$ is the saturated hydraulic**
 339 **conductivity in the vertical direction, θ_r and θ_s are the residual and saturated volumetric**
 340 **water content, α is related to the inverse of the air entry pressure value, and n is soil water**
 341 **retention curve shape parameter.**

| Soil Type | Permeability, k (m^2) | $K_{s,z}$ (cm/hr) | van Genuchten-Mualem Parameters | | | |
|--------------------------------------|--------------------------------|----------------------|---------------------------------|------------------------|----------------|----------------|
| | | | n (-) | α (cm^{-1}) | θ_r (-) | θ_s (-) |
| Top Layer - Modified Loam | 4.8×10^{-14} | 0.17 | 1.31 | 0.019 | 0.095 | 0.43 |
| Claypan | 1.4×10^{-14} | 0.05 | 1.09 | 0.008 | 0.068 | 0.48 |
| Silt Loam | 1.3×10^{-13} | 0.45 | 1.41 | 0.02 | 0.067 | 0.46 |
| Sandy Loam | 1.3×10^{-12} | 4.4 | 1.89 | 0.075 | 0.065 | 0.41 |

342

343

344 4.4. Geochemical System

345 The key geochemical processes included in this study are aqueous speciation, ion
 346 exchange, mineral precipitation/dissolution reactions, and microbially mediated redox reactions.
 347 The primary species in the modeled reaction network include H^+ , H_2O , $SiO_2(aq)$, Na^+ , K^+ , Ca^{+2} ,
 348 Mg^{+2} , HCO_3^- , SO_4^- , Cl^- , $O_2(aq)$, HS^- , NO_3^- , NO_2^- , $N_2(aq)$, $NH_3(aq)$, Al^{+3} , Fe^{+3} , Fe^{+2} , Ba^{+2} , Sr^{+2} , and
 349 acetate. The aqueous complexation reactions and their equilibrium constants are listed in Table
 350 A1 in the Appendix.

351 The mineralogy of the agricultural field site (types and amounts of minerals constituting
 352 each soil type) was assigned on the basis of previous studies at nearby field locations with
 353 similar geology (Harden 1987, Neal et al. 1987, White et al. 1996). Based on these studies,
 354 quartz, k-feldspar, albite, montmorillonite, calcite, illite, ferrihydrite, and gibbsite were taken as
 355 the main soil constituents. All of these minerals are considered to react under kinetic constraints.
 356 The thermodynamic and kinetic constraints for mineral precipitation/dissolution reactions are
 357 listed in Tables A2 and A3 in the Appendix. Note that the amount of ferrihydrite in soil was

358 calibrated according to the ferrozine extractions described above, and amounts of other minerals
 359 estimated from the previously cited studies (Table A4).

360 The groundwater composition was taken from analyses reported by Landon and Belitz
 361 (2006) for a groundwater well (MOD-01) located near our study site. For simplicity, the
 362 background recharge from rainfall was assumed to have the same composition as groundwater
 363 except that it was re-equilibrated under atmospheric O₂ and CO₂ conditions prior to infiltration.
 364 In addition, the concentrations of N species in the background recharge were set to values
 365 determined from our own analyses of N at the top of soil cores. The composition of the flood
 366 water was set to that of the background precipitation diluted by a factor of 100 for most
 367 constituents except for Cl⁻¹. Ratios of NO₃⁻ to Cl⁻¹ were used to trace the difference between
 368 dilution and denitrification effects on NO₃⁻.

369 Denitrification and N₂O production were simulated as aqueous kinetic reactions coupled
 370 to the fate of pH, CO₂, Fe, S, NO₃⁻, and NH₄⁺ based on the Spearman correlation analyses
 371 discussed above (p<0.05). Apart from pH and nitrate species, Fe and S have been linked to
 372 denitrification through chemolithoautotrophic pathways (Arora et al. 2016, Carlson et al. 2012)
 373 in addition to heterotrophic denitrification (Butterbach et al. 2013), and are therefore included in
 374 our reaction network. Heterotrophic denitrification of NO₃⁻ to N₂ was represented via a two-step
 375 reduction process of NO₃⁻ to nitrite (NO₂⁻) and NO₂⁻ to dinitrogen (N₂). Additionally,
 376 chemolithoautotrophic reduction of NO₃⁻ to N₂ with Fe (II) and bisulfide (HS⁻) as electron donors
 377 were implemented. Further, dissolved organic carbon (DOC) was observed throughout the nine-
 378 meter profile at our field site, and CO₂ and N₂O profiles showed strong correlation (p<0.05).
 379 Therefore, DOC degradation was simulated using Monod kinetics, although individual DOC
 380 components were not simulated consistent with other modeling studies (Hunter et al. 1998, Arora
 381 et al. 2015). In particular, we considered a single solid phase of cellulose in equilibrium with
 382 acetate as the source of DOC. Parameters for cellulose dissolution were calibrated using the total
 383 organic carbon concentrations obtained for each cluster. Biodegradation of acetate was coupled
 384 to multiple terminal electron acceptors, including NO₃⁻, Fe (III) and SO₄²⁻ which follow the
 385 hierarchical sequence of reduction potential of each constituent implemented by using inhibition
 386 terms that impede lower energy-yielding reactions when the higher energy yielding electron
 387 acceptors are present. These microbially mediated reactions and their kinetic rate parameters are
 388 shown in Table 5.

389 Rates for denitrification were calibrated using the results from the acetylene inhibition
 390 assays as described above. Enzymes involved in denitrification include nitrate reductase, nitrite
 391 reductase and nitrous oxide reductase. To remain conservative in our estimates, we chose values
 392 typical for oxygen inhibition of nitrous oxide reductase (0.01 mg O_{2(aq)} L⁻¹), the most sensitive to
 393 oxygen of the enzymes (Bonin et al. 1989).

395 **Table 4: Microbially mediated redox reactions, their thermodynamic and kinetic**
 396 **parameters considered in the reactive transport model.**

| Reaction | Log K (25 °C) ^(a) | K _{max} (mol L ⁻¹ s ⁻¹) | K _s (mol L ⁻¹) | K _{inhibitor} (mol L ⁻¹) |
|----------|------------------------------------|---|--|--|
| | | | | |

| | | | | |
|--|--------|----------------------------|--|---|
| $\text{CH}_3\text{COO}^- + 2\text{O}_2 \rightarrow 2\text{HCO}_3^- + \text{H}^+$ | 146.76 | 1.0×10^{-11} (b) | $\text{O}_2: 2.41 \times 10^{-5}$ (d) | |
| $\text{CH}_3\text{COO}^- + 4\text{NO}_3^- \rightarrow 2\text{HCO}_3^- + 4\text{NO}_2^- + \text{H}^+$ | 89.04 | 2.78×10^{-10} (c) | $\text{NO}_3^-: 1.13 \times 10^{-4}$ (d) | $\text{O}_2: 3.22 \times 10^{-7}$ (e) |
| $\text{CH}_3\text{COO}^- + 2.667\text{NO}_2^- + 1.667\text{H}^+ \rightarrow 2\text{HCO}_3^- + 1.33\text{N}_2 + 1.33\text{H}_2\text{O}$ | 200.52 | 3.47×10^{-8} (c) | $\text{NO}_2^-: 1.13 \times 10^{-4}$ (d) | $\text{O}_2: 3.22 \times 10^{-7}$ (e) |
| $\text{NH}_3(\text{aq}) + 2\text{O}_2 \rightarrow \text{NO}_3^- + \text{H}_2\text{O} + \text{H}^+$ | 62.23 | 5.27×10^{-2} (b) | $\text{NH}_3: 1.48 \times 10^{-5}$ (f) $\text{O}_2: 2.41 \times 10^{-5}$ (d) | |
| $\text{CH}_3\text{COO}^- + 8\text{Fe}^{+3} + 4\text{H}_2\text{O} \rightarrow 8\text{Fe}^{+2} + 2\text{HCO}_3^- + 9\text{H}^+$ | 79.00 | 1.0×10^{-14} (b) | | $\text{O}_2: 3.22 \times 10^{-7}$ (e) $\text{NO}_3^-: 1.0 \times 10^{-7}$ (g) |
| $\text{Fe}^{+2} + 0.2\text{NO}_3^- + 1.2\text{H}^+ \rightarrow \text{Fe}^{+3} + 0.1\text{N}_2 + 0.6\text{H}_2\text{O}$ | -7.32 | 7.0×10^{-10} (h) | $\text{Fe}^{+2}: 1.0 \times 10^{-5}$ (i) $\text{NO}_3^-: 1.13 \times 10^{-4}$ (d) | $\text{O}_2: 3.22 \times 10^{-7}$ (e) $\text{NO}_3^-: 1.0 \times 10^{-7}$ (g) |
| $\text{CH}_3\text{COO}^- + \text{SO}_4^{-2} \rightarrow 2\text{HCO}_3^- + \text{HS}^-$ | 8.40 | 3.0×10^{-12} (b) | $\text{SO}_4^{-2}: 1.0 \times 10^{-3}$ (j) | $\text{O}_2: 3.22 \times 10^{-7}$ (e) $\text{NO}_3^-: 1.0 \times 10^{-7}$ (g) $\text{Fe}^{+3}: 1.0 \times 10^{-12}$ (b) |
| $\text{HS}^- + 1.6\text{NO}_3^- + 0.6\text{H}^+ \rightarrow \text{SO}_4^{-2} + 0.8\text{N}_2 + 0.8\text{H}_2\text{O}$ | 11.52 | 7.0×10^{-10} (j) | $\text{HS}^-: 1.0 \times 10^{-5}$ (k) $\text{NO}_3^-: 1.13 \times 10^{-4}$ (d) | $\text{O}_2: 3.22 \times 10^{-7}$ (e) |

397
 398 (a) Calculated from logK values for half redox reactions reported by (Morel and Hering 1993); (b) Adapted from Arora et al. 2016;
 399 (c) Calibrated using denitrification capacity assays; (d) Taken from Maggi et al. 2008; (e) Taken from Bonin et al. 1989; (f) Taken from
 400 Wu et al. 2011; (g) Taken from Doussan et al. 1997; (h) Adapted from Palmer et al. 2010; (i) Taken from Mayer et al. 2002; (j) Kept
 401 to yield maximum reaction rate similar to that of NO_3^- reduction by Fe^{+2} ; (k) Taken from Handley et al. 2013
 402

403 5. Results

404 5.1. Cluster Analysis

405 Cluster analysis was used to detect natural groupings in the soil data based on physio-chemical
 406 characteristics, textural classes and the total dataset. Cluster analysis revealed three clusters
 407 representing distinct depth associated textural classes with varying levels of substrates and
 408 biogeochemical activity. Table 6 shows the median and range for N_2O , CO_2 , NO_3^- -N, Fe, S and
 409 total organic C for each of the clusters. The first cluster is dominated by sandy loams within the
 410 top meter with highest median values of total N_2O , total CO_2 , NO_3^- -N, Fe, and total organic C
 411 concentrations, indicative of greatest microbial activity and denitrification potential. The second
 412 cluster is dominated by silt loams below one meter and had average values of total N_2O , total
 413 CO_2 , NO_3^- -N, Fe, and total organic C concentrations when compared to the other groups. The
 414 third group is dominated by sands and sandy loams below 1 meter and had the lowest median
 415 values of total N_2O , total CO_2 , NO_3^- -N, Fe, and total organic C concentrations amongst all
 416 groups. The clusters were thus automatically grouped by decreasing levels of denitrification and
 417 microbial activity. While most concentrations followed a decreasing concentration trend from
 418 cluster 1 to 3, the highest median values of S were associated with cluster 2.
 419

420 **Table 5: Results of cluster analysis on soil core and acetylene inhibition incubation data.**
 421 **Medians are shown with minimum and maximum values in parentheses.**

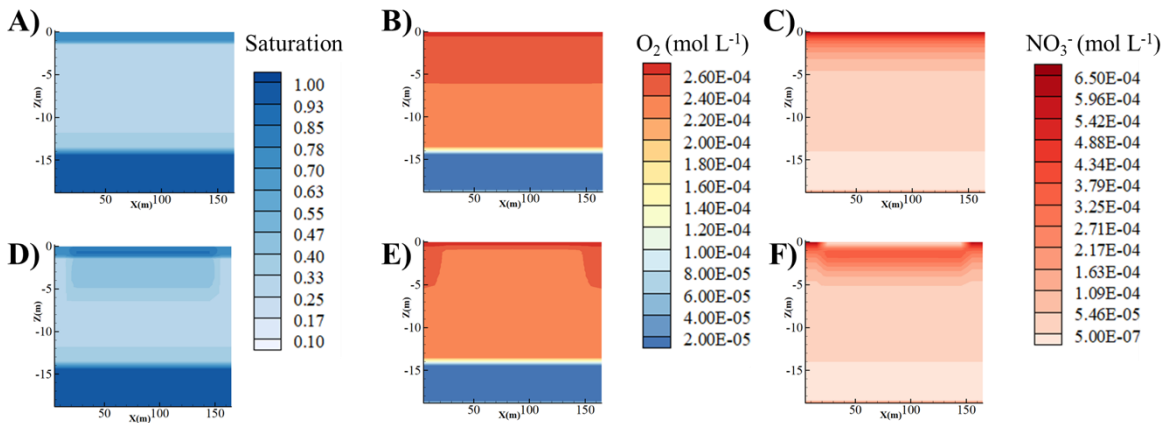
| | Soil Classification | Total N₂O | Total CO₂ | TOC | NO₃⁻ | Fe | S |
|---|-------------------------------------|-----------------------------|-----------------------------|--------------------|-----------------------------------|--------------------------|--------------------------|
| | | ug g⁻¹ | ug g⁻¹ | % | ug g⁻¹ | ug g⁻¹ | ug g⁻¹ |
| 1 | Sandy Loam top meter | 1.62 (1.46-1.72) | 175.30 (74.70-587.35) | 0.18 (0.01 - 0.29) | 1.20 (1.19 - 2.64) | 14.77 (10.94 - 20.66) | 0.44 (0.33 - 0.47) |
| 2 | Silt Loam below one meter | 0.53 (0.40 - 0.80) | 35.70 (15.10 - 61.97) | 0.07 (0.03 - 0.16) | 1.01 (0.80 - 1.84) | 12.02 (8.64 - 14.96) | 0.69 (0.41 - 1.20) |
| 3 | Sand and Sandy Loam below one meter | 0.05 (0.01 - 0.015) | 10.70 (0.0 - 59.40) | 0.06 (0.03 - 0.10) | 0.25 (0.0 - 0.70) | 10.43 (7.27-16.34) | 0.44 (0.24 - 1.01) |

422

423 **5.2. Reactive Transport Model Simulations**

424 **5.2.1. Simulated base case conditions and results from scenario S1**

425 Liquid saturation profiles and concentration of key aqueous species predicted at different
 426 times for the homogeneous sandy loam column are shown in Figure 5. The sandy loam vadose
 427 zone is computed to be 32% saturated with near atmospheric concentrations of O₂. As a result of
 428 oxic conditions, model results demonstrate significant residual NO₃⁻ concentration within the
 429 vadose zone (as would be expected). Evolving from these conditions, Figure 5 shows that with
 430 flooding scenario S1, water reaches depths of 490 cm and saturation levels reach 40% in the
 431 sandy loam column. Deeper in the column, lower saturation and only small decreases in O₂
 432 concentration are predicted (Figure 5d, e). Calculated concentration profiles show that O₂
 433 introduced with the infiltrating water is persistent at shallow depths down to 100 cm, below
 434 which O₂ declines slightly as floodwater moves below this zone. Model results further indicate
 435 higher NO₃⁻ reduction in the shallow vadose zone including the root zone (up to 100cm) with
 436 35% of NO₃⁻ being denitrified (Figure 5f). Overall, this scenario results in NO₃⁻ concentration
 437 persisting at depth. While other redox reactions, such as iron reduction and HS⁻ reduction of
 438 NO₃⁻ to N₂, may be important, conditions needed to induce these reactions were not realized in
 439 the sandy loam vadose zone due to the high pore gas velocities of the homogenous sandy loam
 440 allowing for large amounts of O₂ to penetrate the profile from the incoming oxygenated water.



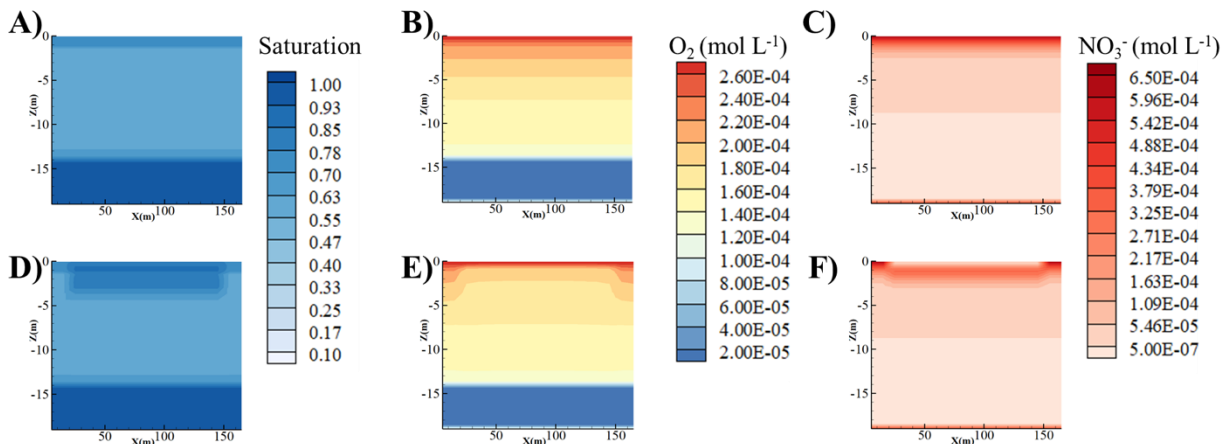
441
442
443
444
445

Figure 5: Homogeneous Sandy Loam: Predicted liquid saturation, O₂ (mol L⁻¹), and NO₃⁻ (mol L⁻¹) profiles at pre-flood steady state (A, B, and C, respectively) and 60 days from start of flooding for S1 (D, E, F).

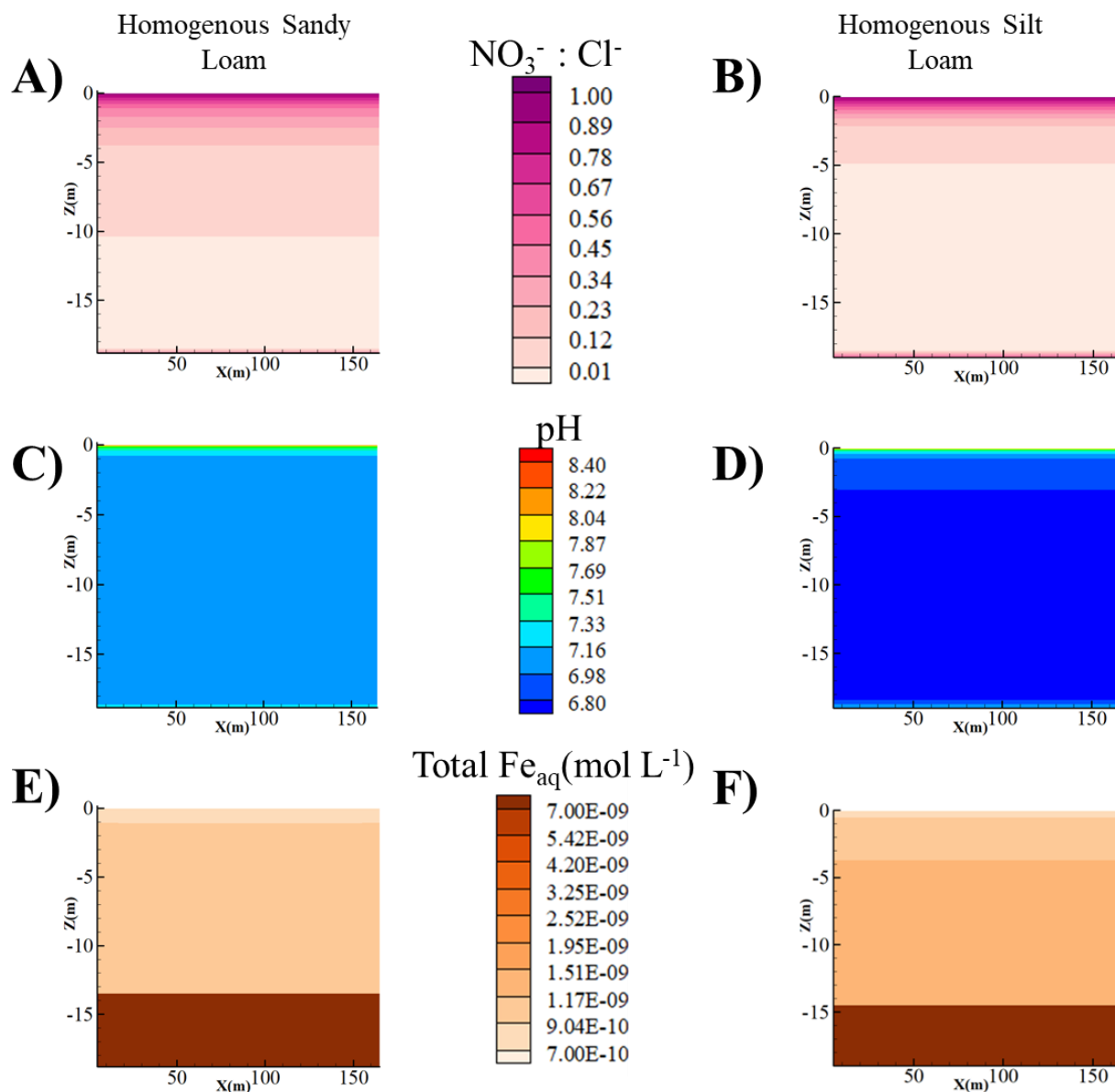
446
447
448
449
450
451
452
453
454
455
456
457
458
459
460
461
462
463
464
465
466

In comparison to the homogenous sandy loam column, the predicted water content is higher (60% saturated) and O₂ concentration is 53% lower in the vadose zone of the homogenous silt loam column at steady state (Figure 6). This result is expected because of the difference in porosity, with silt loams having higher water holding capacity and lower pore gas velocities compared to sandy loams. Consequently, lower NO₃⁻ concentration and lower NO₃⁻:C:I ratio are predicted in the silty loam vadose zone as compared to the sandy loam column (Figures 6 and 7). It is interesting to note that while greater NO₃⁻ loss and denitrification are predicted for the silty loam vadose zone, carbon concentration associated with the shallow vadose zone (below the root zone) are comparatively lower than for the sandy loam column. Moreover, the calculated pH is lower and iron concentrations are higher in the silt loam profile below the top meter when compared to the same depths within the sandy loam column (Figure 7). This suggests that chemolithoautotrophic reactions could be more important for these finer textured sediments. While both heterotrophic and chemolithoautotrophic reactions would be expected to result in a pH decrease (as expressed in Table 5), the greater decline in pH and concomitant increase in Fe⁺³ concentration suggests the importance of Fe and S redox cycling associated with the chemolithoautotrophic reactions in silty loam sediments (Figure 7).

Evolving from these steady state conditions, scenario S1 suggests that denitrification is enhanced as floodwater infiltrates into the silt loam column. Model results indicate that saturation increases to 80% from 1 to 4 m depths and O₂ decreases from 2.1 x 10⁻⁴ mol L⁻¹ to 1.7 x 10⁻⁴ mol L⁻¹, resulting in 43% of the NO₃⁻ being denitrified for this scenario (Figure 8).



467
 468 **Figure 6: Homogeneous Silt Loam: Predicted liquid saturation, O_2 (mol L^{-1}), and NO_3^- (mol**
 469 **L^{-1}) profiles at pre-flood steady state (A, B, and C, respectively) and 60 days from start of**
 470 **flooding for S1 (D, E, F).**

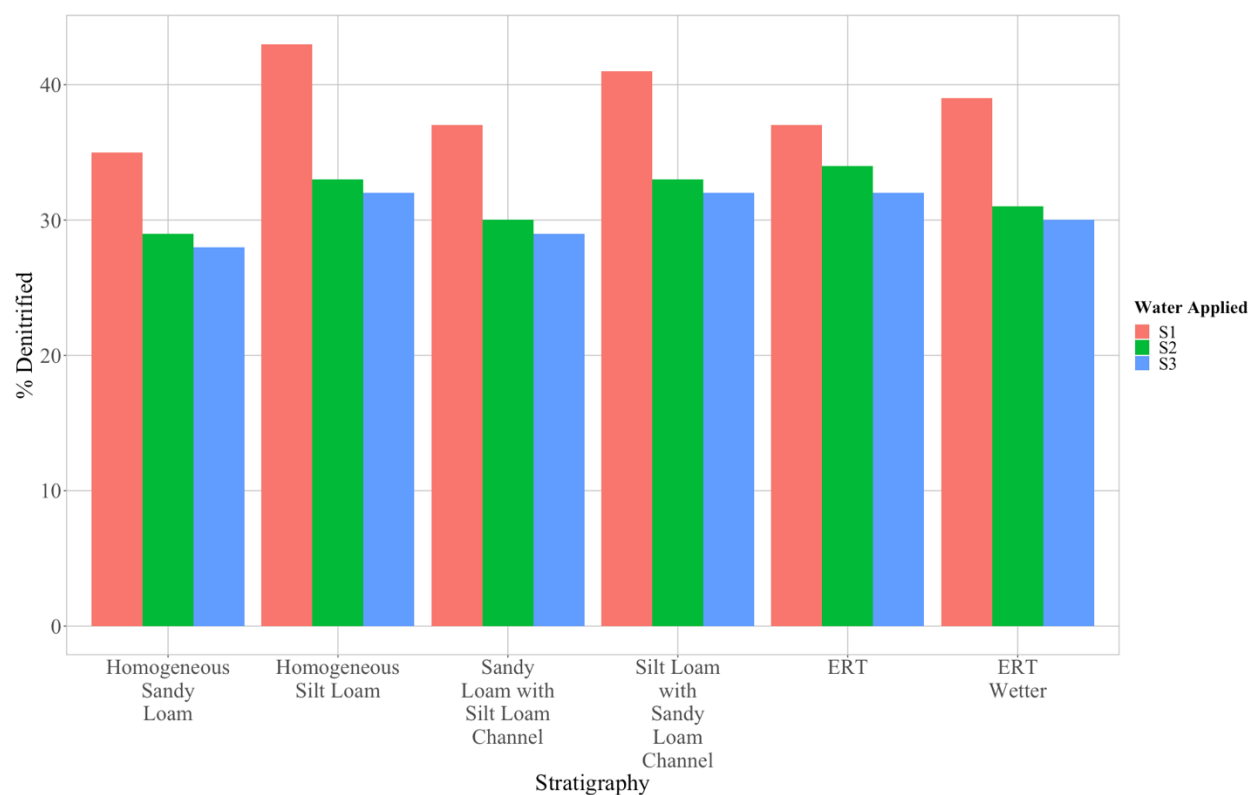


471

472

473 **Figure 7: Predicted $NO_3^-:Cl^-$ (A and B), pH (C and D), and total Fe_{aq} (E and F) (mol L⁻¹),**
 474 **and total Fe_{aq} (G and H) (mol L⁻¹) profiles for the homogeneous sandy loam vs.**
 475 **homogeneous silt loam stratigraphies at pre-flood steady state.**

476

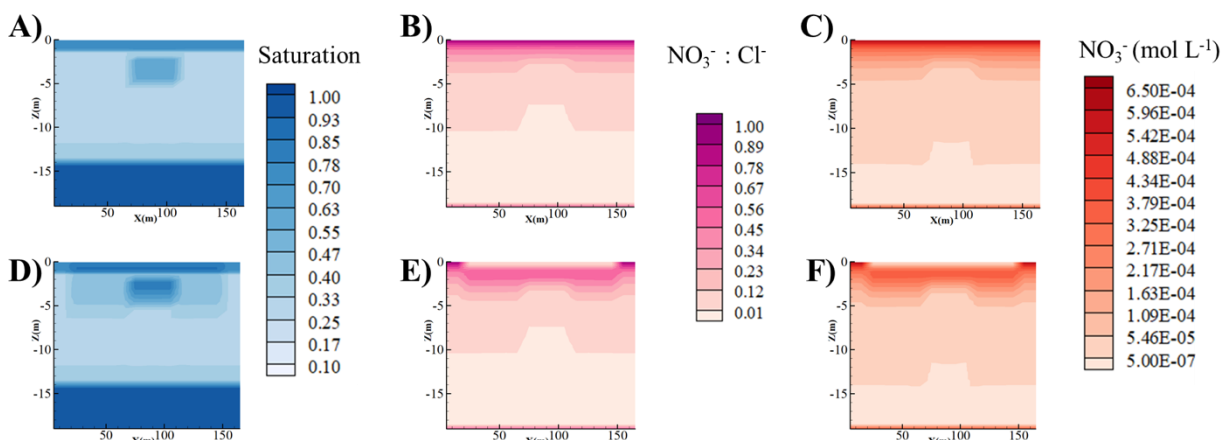


477

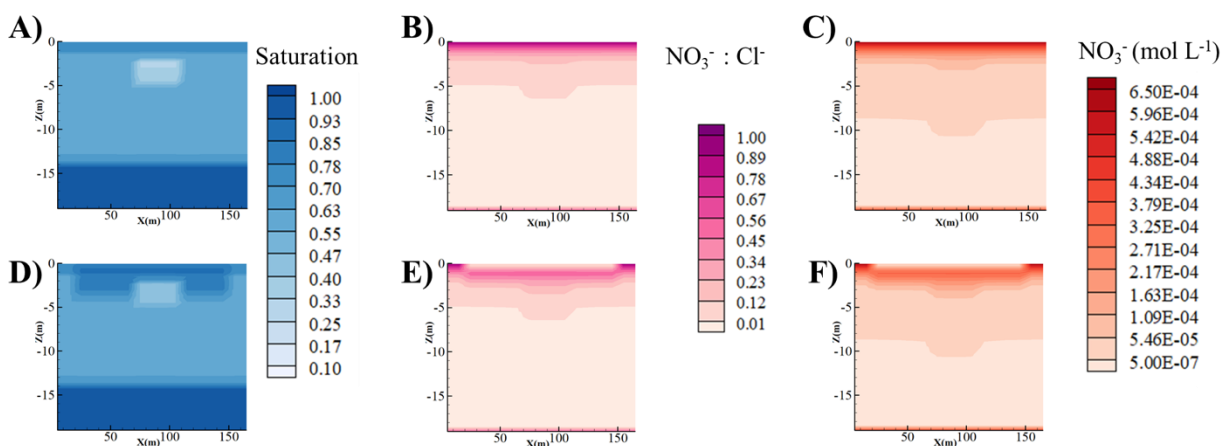
478 **Figure 8: Percent of NO_3^- denitrified for each stratigraphy and flooding scenario.**

479

480 In comparison to the homogeneous profiles, the sandy loam with silt loam channel
 481 stratigraphy (SaSi case) has higher calculated water contents (60% saturated) and slightly lower
 482 O_2 concentration within and surrounding the silt loam channel than the homogenous sandy loam
 483 column under steady state conditions (Figure 9). Calculated NO_3^- concentrations are also similar
 484 between the homogenous sandy loam column and SaSi case, except for within and below the silt
 485 loam channel where lower NO_3^- concentration was predicted (Figure 9). For scenario S1, water
 486 content for the SaSi case increased in a manner similar to the homogenous sandy loam, except
 487 for within the silt loam channel, which increased from 60 to 81%. Figure 9 further demonstrates
 488 that the infiltrating floodwater resulted in an increase in NO_3^- concentration between 1 and 3 m
 489 within the sandy loam textured soil, but a decrease elsewhere. Within the channel itself, lower
 490 nitrate and $\text{NO}_3^-:\text{Cl}^-$ ratio are predicted, suggesting higher rates of denitrification (Figure 9).
 491 Overall, the model results indicate that an average of 37% of the NO_3^- concentration is
 492 denitrified in the SaSi case, with 35% denitrification occurring in the sandy loam matrix and
 493 40% occurring within the silt loam channel. This suggests that the silt loam channel acts as a
 494 denitrification hotspot. Furthermore, the silt loam channel has lower carbon and higher Fe^{+3}
 495 concentrations similar to the homogenous silt loam column again suggesting the importance of
 496 both heterotrophic and chemolithoautotrophic denitrification in these finer textured sediments.
 497



498
499 **Figure 9: Sandy loam with silt loam channel (SaSi case) predicted liquid saturation, NO_3^-**
500 **: Cl^- ratios, and NO_3^- (mol L^{-1}) profiles at pre-flood steady state (A, B, and C, respectively)**
501 **and 60 days from start of flooding for S1 (D, E, F).**

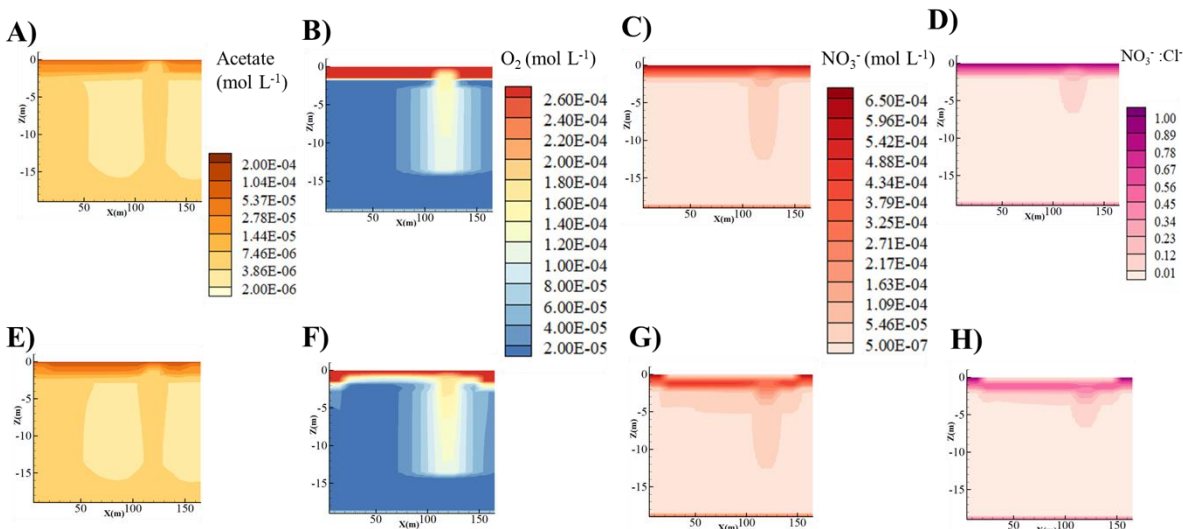


502
503 **Figure 10: Silt loam with sandy loam channel (SiSa case) predicted liquid saturation, NO_3^-**
504 **: Cl^- ratios, and NO_3^- (mol L^{-1}) profiles at pre-flood steady state(A, B, and C, respectively)**
505 **and 60 days from start of flooding for S1 (D, E, F).**

506 In comparison to the SaSi case, calculated water saturation and O_2 profiles were
507 markedly different between the homogenous silt loam column and the silt loam with sandy loam
508 channel (SiSa case) under steady state conditions (Figure 10). In particular, the sandy loam
509 channel has lower calculated water content (32% saturation) than the homogenous silt loam
510 column (60% saturation). Further, greater gas flux within the channel resulted in 11-19% higher
511 O_2 concentration that penetrated deeper into the vadose zone as compared to the homogeneously
512 textured column. NO_3^- concentration are also estimated to penetrate deeper into the vadose zone
513 in the SiSa case due to the high permeability of the sandy loam channel (Figure 10). While
514 carbon concentration also penetrated deeper in the vadose zone in the SiSa case, higher
515 calculated O_2 concentration did not allow for comparable rates of denitrification in this case as
516 observed in the homogenous silt loam profile. This is further confirmed by the lower $\text{NO}_3^-:\text{Cl}^-$
517 ratio, which indicates that transport processes dominate biogeochemical fluxes within this

518 column (Figure 10). With scenario S1, the calculated water content increased to 48% saturation
 519 while the O₂ concentration remained the same within the channel. The high permeability channel
 520 allowed for NO₃⁻ to move faster and deeper into the vadose zone. Overall, calculated
 521 denitrification (41% of NO₃⁻ was denitrified) was lower in the SiSa case as compared to the
 522 homogeneous textured column.

523 In the simplified ERT stratigraphy, similar patterns were observed such that high
 524 permeability channels transported water, O₂, and NO₃⁻ faster and deeper into the subsurface than
 525 low permeability regions (Figure 11). As a result, concentration profiles showed significant
 526 variability across the modeled domain even under steady state conditions. For example, the
 527 calculated O₂ and NO₃⁻ concentrations are an order of magnitude lower in the shallow vadose
 528 zone below the claypan than within the preferential flow channel. Higher NO₃⁻:Cl⁻ ratio within
 529 the channel further confirms that preferential flow paths transport higher quantities of dissolved
 530 aqueous species without their being impacted by other processes such as denitrification (Figure
 531 11). Other interesting trends are shown by carbon and Fe⁺² concentrations within the modeled
 532 column. Dissolved carbon in particular is predicted to have a lower concentration in the
 533 preferential flow channel and the matrix surrounding the channel than below the claypan layer.
 534 In contrast, the Fe⁺² concentration is estimated to be higher in the matrix surrounding the
 535 preferential flow channel and below the claypan layer (not shown here). For scenario S1, model
 536 results indicate that NO₃⁻ moved through the preferential flow path faster and deeper into the
 537 profile, while the claypan acts as a denitrification barrier as evidenced by the decrease in NO₃⁻
 538 :Cl⁻ ratio. The highest denitrification was estimated to occur in the matrix adjacent to the
 539 preferential flow channel (40% of NO₃⁻), followed by intermediate nitrate reduction below the
 540 claypan and far away from the channel (38%), while the lowest denitrification was estimated to
 541 occur within the channel itself (34%). The confluence of higher amounts of C and NO₃⁻ moving
 542 into a reduced zone could be the reason that the matrix surrounding the preferential flow channel
 543 has higher denitrification rates, while the regions further away from the preferential flow channel
 544 have lower amounts of microbially available C and NO₃⁻. In contrast, residence times are too
 545 short in the channel to allow for reducing conditions to develop. Overall, we find that low
 546 permeability zones alone (e.g., homogeneous silt loam) embedded within high flow zones (eg.,
 547 matrix surrounding preferential flow channel, SiSa case) demonstrate highest denitrification rates
 548 across all soil profiles.



549
 550 **Figure 11: Simplified ERT predicted acetate (mol L⁻¹), O₂ (mol L⁻¹), NO₃⁻ (mol L⁻¹)**
 551 **profiles, NO₃⁻:Cl⁻ ratios at pre-flood steady state (A, B, C, and D respectively) and 60 days**
 552 **from start of flooding for S1 (E, F, G and H).**

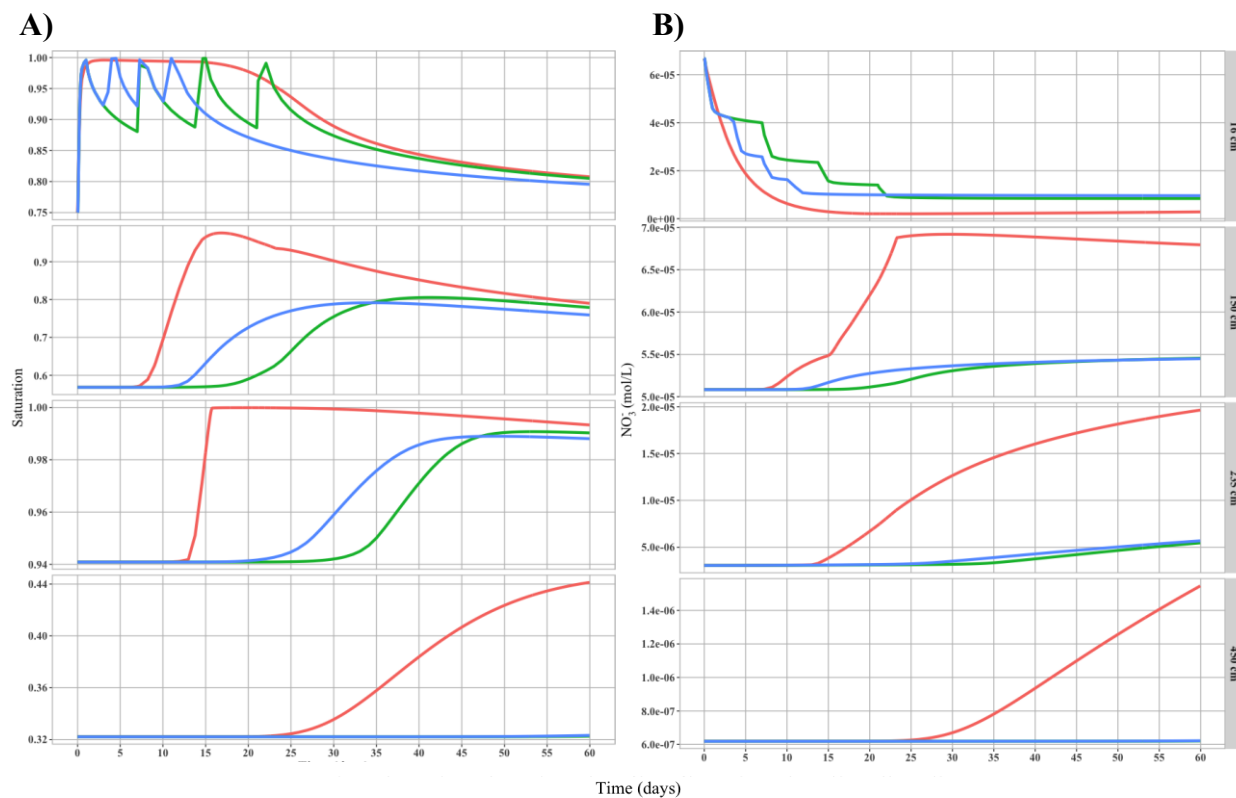
553

554 **5.2.2. Results from scenarios S2 and S3**

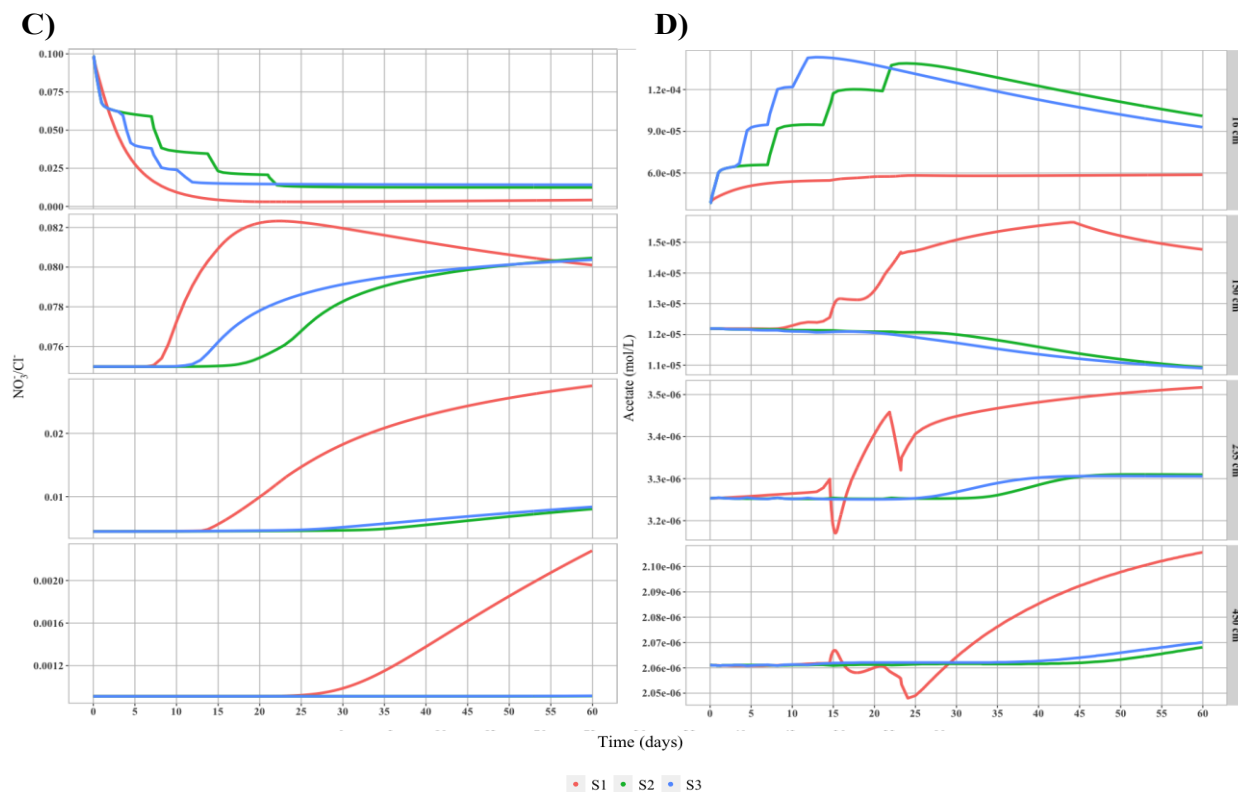
555 Because the ERT column is a realistic representation of our agricultural field site, we use
 556 this column to demonstrate the impact of hydraulic loading and application frequency on
 557 nitrogen fate and dynamics. Simulated profiles of liquid saturation, NO₃⁻, NO₃⁻:Cl⁻ and acetate
 558 for the simplified ERT stratigraphy for scenarios S2 (17 cm per week for four weeks) and S3 (17
 559 cm two times per week for two weeks) are shown in Figure 12. It is interesting to note that
 560 AgMAR ponding under scenarios S2 and S3 resulted in fully saturated conditions to persist
 561 within the root zone (~ 100 cm depths) only. In comparison, the 68 cm all-at-once application for
 562 scenario S1 resulted in fully saturated conditions to occur at even greater depths of 235 cm (not
 563 shown here). This resulted in the NO₃⁻ front moving deeper into the subsurface to depths of 450
 564 cm under S1 compared to 150 cm for scenarios S2 and S3 (Figure 12). Much lower
 565 concentrations of NO₃⁻ were found at 450 cm in scenarios S2 and S3 (8 x 10⁻⁶ mol NO₃⁻ L for
 566 both S2 and S3) compared to S1 (1 x 10⁻⁵ mol NO₃⁻ L). Thus, larger amounts of water applied all-
 567 at-once led to NO₃⁻ being transported faster and deeper into the profile.

568 Surprisingly, model results indicate 37% of NO₃⁻ was denitrified with scenario S1, while
 569 34% and 32% of NO₃⁻ was denitrified in scenarios S2 and S3, respectively. For scenarios S2 and
 570 S3, denitrification was estimated to occur only within the root zone. This was confirmed by NO₃⁻
 571 :Cl⁻ ratio that did not show any reduction with depth for these scenarios. A reason for this could
 572 be that acetate was not estimated to occur below the root zone, preventing electron donors from
 573 reaching greater depths for denitrification to occur. In contrast, model results for S1 indicate that
 574 acetate was leached down to 235 cm below the claypan layer. Overall, model results indicate that
 575 NO₃⁻ did not move as fast or as deep in scenarios S2 or S3; however, the ability of the vadose
 576 zone to denitrify was reduced when the hydraulic loading was decreased. The main reason for
 577 this was that breaking the application into smaller hydraulic loadings (17 cm) resulted in O₂
 578 concentrations to recover to background atmospheric conditions faster than the larger (68 cm)

579 all-at-once application in scenario S1. In fact, the O₂ concentration differed slightly between S2
 580 and S3. Because O₂ inhibits denitrification, we conclude that these conditions resulted in the
 581 different denitrification capacity across application frequency and duration. In summary, we find
 582 that larger amounts of water applied all-at-once increased the denitrification capacity of the
 583 vadose zone while incremental application of water did not. However, NO₃⁻ movement to deeper
 584 depths was slower under S2 and S3.
 585



586



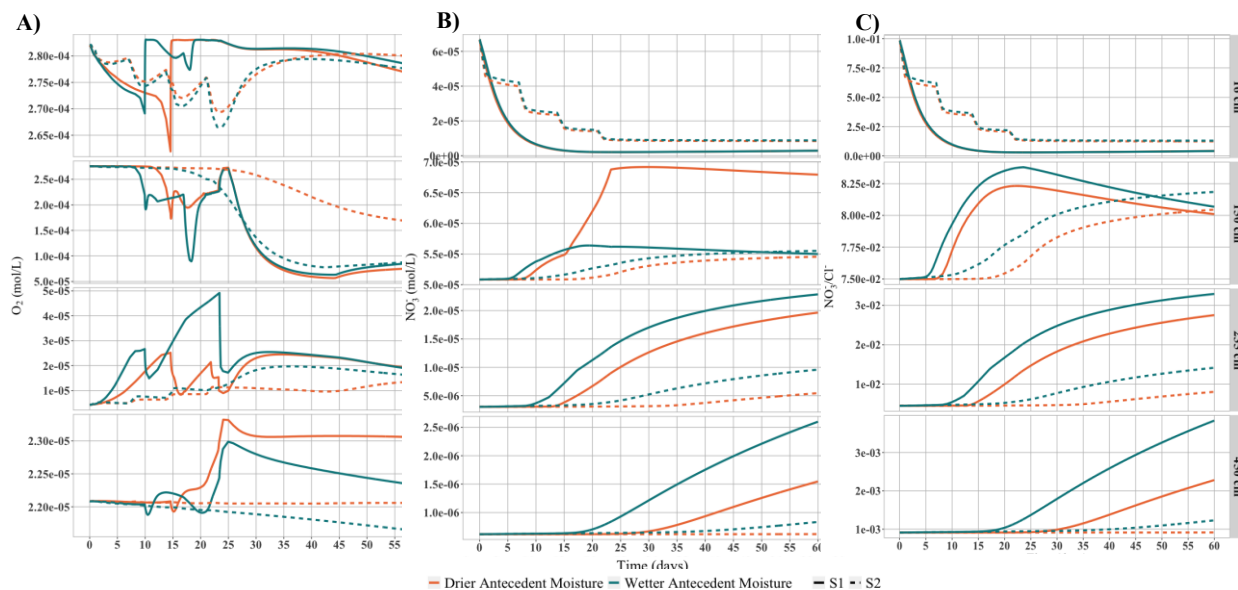
587
 588 **Figure 12: A) Saturation, B) NO_3^- (mol L^{-1}), C) ratio of NO_3^- to Cl^- and D) Acetate**
 589 **concentrations (mol L^{-1}), and over time by depth within each AgMAR scenario(S1, S2, S3)**
 590 **adjacent to the preferential flow channel for the Simplified ERT profile.**

591 **5.2.3. Results from varying Antecedent Moisture conditions**

592 Because initial saturation conditions impact nitrogen leaching, we also simulated the
 593 impact of wetter antecedent moisture with 15% higher saturation levels than the base case
 594 simulation for the ERT profile. Simulated profiles of liquid saturation, NO_3^- , $\text{NO}_3^-:\text{Cl}^-$ and
 595 acetate for the simplified ERT stratigraphy under wetter conditions are shown in Figure 13.
 596 Model results demonstrate that the water front moved faster and deeper into the soil profile under
 597 initially wetter conditions for all three scenarios. Within the shallow vadose zone (~150 cm),
 598 across AgMAR scenarios, O_2 concentrations were similar initially, but began differing at early
 599 simulated times, with lower O_2 under wetter antecedent moisture conditions than with the base-
 600 case simulation. In addition, both oxygen and nitrate concentrations showed significant spatial
 601 variation across the modeled column. Notably, nitrate concentrations were 166% (order of
 602 magnitude) higher in the preferential flow channel compared to the sandy loam matrix under
 603 wetter conditions, while only 161% difference was observed under the base case simulation
 604 (Figure 13).

605 Nitrate movement followed a pattern similar to water flow, with NO_3^- reaching greater
 606 depths with the wetter antecedent moisture conditions. Under S1, however, at 150 cm, NO_3^-
 607 decreased more quickly under the wetter antecedent moisture conditions due to biochemical
 608 reduction of NO_3^- , as evidenced by the decrease in $\text{NO}_3^-:\text{Cl}^-$ ratio, as well as by dilution of the
 609 incoming floodwater. In the wetter antecedent moisture conditions, 39%, 31%, and 30% of NO_3^-

610 was denitrified under S1, S2, and S3, respectively. For S1, where water was applied all at once,
 611 more denitrification occurred in the wetter antecedent moisture conditions, however, the same
 612 was not true of S2 and S3 where water applications were broken up over time. This could be due
 613 to the hysteresis effect of subsequent applications of water occurring at higher initial moisture
 614 contents, allowing the NO_3^- to move faster and deeper into the profile without the longer
 615 residence times needed for denitrification to occur. Thus, wetter antecedent moisture conditions
 616 prime the system for increased denitrification capacity when water is applied all at once and
 617 sufficient reducing conditions are reached, however, this is counteracted by faster movement of
 618 NO_3^- into the vadose zone.
 619



620
 621
 622 **Figure 13: A) O_2 (aq) concentrations (mol L⁻¹), B) NO_3^- (mol L⁻¹), and C) ratio of NO_3^- to Cl^-**
 623 **over time by depth within AgMAR scenarios (S1 and S2) for different antecedent moisture**
 624 **conditions adjacent to the preferential flow channel.**

625

626 6. Discussion

627 6.1. Impact of Stratigraphy

628 Because several characteristics of the vadose zone add complexity to modeling and
 629 understanding N cycling in agricultural soils, we used a reactive transport modeling framework
 630 to isolate and elucidate the effect of varying stratigraphic configurations and sediment types on N
 631 transformation and denitrification. Our results primarily demonstrate that low-permeability zones
 632 such as silt loams allow for reducing conditions to develop, thereby leading to higher
 633 denitrification in these sediments as compared to high permeability zones such as sandy loams.
 634 In fact, the homogenous silt loam profile reported the maximum amount of denitrification
 635 occurring across all five stratigraphic configurations (Figure 8). Furthermore, the presence of a
 636 silt loam channel in a dominant sandy loam column increased the capacity of the column to

637 denitrify by 2%. Conversely, adding a sandy loam channel into a silt loam matrix decreased the
638 capacity of the column to denitrify by 2%. These relatively simple heterogeneities exemplify
639 how hot spots in the deep vadose zone can have a small but accumulating effect on
640 denitrification capacity.

641 Another observation of interest for silty loams is the prominence of
642 chemolithoautotrophic reactions and Fe cycling observed in these sediments. In comparison,
643 sandy loam sediments showed persistence and transport of NO_3^- to greater depths. A reason for
644 this is that oxygen concentration was much more dynamic in sandy loams, rebounding to oxic
645 conditions more readily than in silt loams, even deep into the vadose zone (5 meters). Dutta et al.
646 (2015) found similar re-aeration patterns in a 1 m column experiment in a sand dominated soil,
647 with re-aeration occurring quickly once drying commenced. Even with the presence of a claypan,
648 defined by lower pore gas velocities and higher carbon concentration, a sandy loam channel
649 acted as a conduit of O_2 into the deep vadose zone maintaining a relatively oxic state and thus
650 decreasing the ability of the vadose zone to denitrify. Overall, denitrification capacity across
651 different lithologies was shown to depend on the tight coupling between transport, biotic
652 reactions as well as the cycling of Fe and S through chemolithoautotrophic pathways.

653

654 **6.2. Impact of Hydraulic Loading and Frequency**

655 Our results demonstrate that both hydraulic loading and frequency influenced the depth to
656 which NO_3^- reached, as well as the denitrification capacity of the subsurface. Given legacy
657 nitrate contamination is prevalent within the root zone of agricultural soils, we quantified the
658 amount of NO_3^- being lost from this zone across different loadings and duration of floodwater
659 application. Note that the root zone was made of the same soil texture across different
660 stratigraphic configurations, and accounted for a large proportion of denitrification in the system.
661 Under large hydraulic loadings (i.e., S1), lower denitrification was estimated in the root zone as
662 compared to the lower hydraulic loading scenarios (i.e., S2 or S3). However, overall
663 denitrification was estimated to be greatest under S1 when 68 cm of water was applied all-at-
664 once. The main reason for the higher denitrification capacity was the significant decline in O_2
665 concentration estimated for this scenario, whereas such conditions could not be maintained
666 below one meter with lower hydraulic loadings under scenarios S2 and S3. It seems that there
667 may exist a threshold hydraulic loading and frequency of application that could result in anoxic
668 conditions and therefore promote denitrification within the vadose zone for different
669 stratigraphic configurations, although this was not further explored in this study. In another
670 study, Schmidt et al. (2011) found a threshold infiltration rate of 0.7 m d^{-1} for a three-hectare
671 recharge pond located in the Pajaro Valley of central coastal California, such that no
672 denitrification occurred when this threshold was reached.

673 Our results further indicate that higher hydraulic loading, in addition to causing increased
674 levels of saturation and decrease in O_2 , resulted in leaching of DOC to greater depths in
675 comparison to lower hydraulic loading scenarios (i.e., S2, S3). Akhavan et al. 2013 found similar
676 results for an infiltration basin wherein 1.4% higher DOC levels were reported at depths down to
677 4 m when hydraulic loading was increased. Because organic carbon is typically limited to top 1
678 m in soils (Dwivedi et al., 2018), leached DOC that has not been microbially processed could be
679 an important source of electron donors for denitrification at depth. This finding can be exploited

680 in agricultural soils by using cover crop and other management practices that increase soluble
681 carbon at depth and therefore remove residual N from the vadose zone.

682 While lower denitrification capacity was estimated for scenarios S2 and S3, an advantage
683 of incremental application was that NO_3^- concentration was not transported to greater depths.
684 Thus, higher NO_3^- concentration was confined to the root zone. If NO_3^- under these scenarios
685 stays closer to the surface, where microbial biomass is higher, and where roots, especially in
686 deep rooted perennial systems such as almonds, can access it, it could ultimately lead to less
687 NO_3^- lost to groundwater. While there is potential for redistribution of this NO_3^- via wetting and
688 drying cycles, future modeling studies should explore multi-year AgMAR management
689 strategies combined with root dynamics to understand N cycling under long-term AgMAR.

690 **6.3. Impact of Antecedent Moisture**

691 Simulation results indicate that wetter antecedent moisture conditions promote water and
692 NO_3^- to move deeper into the domain compared to the drier base case simulation. This finding
693 has been noted previously in the literature, however, disagreement exists on the magnitude and
694 extent to which antecedent moisture conditions affect water and solute movement and is highly
695 dependent on vadose zone characteristics. For example, in systems dominated by macropore
696 flow, higher antecedent soil moisture increased the depth to which water and solutes were
697 transported (McCoy et al. 1994, Jarvis et al. 2007). In a soil with textural contrast, where
698 hydraulic conductivity between the topsoil and subsoil decreases sharply, drier antecedent
699 moisture conditions caused water to move faster and deeper into the profile compared to wetter
700 antecedent moisture conditions (Hardie et al. 2011). In our system, where a low-permeability
701 layer (i.e., claypan) lies above a high permeability layer (i.e., sandy loam), the reverse trend was
702 observed. Thus, a tight coupling of stratigraphic heterogeneity and antecedent moisture
703 conditions interact to affect both NO_3^- transport and cycling in the vadose zone, which should be
704 considered while designing AgMAR management strategies to reduce NO_3^- contamination of
705 groundwater.

706 **7. Conclusion**

707 Agricultural managed aquifer recharge is a promising management strategy to increase
708 groundwater recharge. However, to ensure adoption of the practice, AgMAR must not
709 compromise groundwater quality. To quantify the influence of AgMAR on groundwater quality,
710 specifically nitrate, we tested different AgMAR application rates under different stratigraphic
711 configurations and antecedent moisture conditions using a reactive transport modeling
712 framework. Our results indicate that fine textured sediments by themselves (e.g., homogeneous
713 silt loam) or embedded within high permeability zones (e.g., silt loam channel within sandy loam
714 sediments, matrix surrounding preferential flow channels) demonstrate highest denitrification
715 capacity across different stratigraphic configurations. Further, in comparing AgMAR strategies,
716 we found that denitrification capacity increased by applying large amounts of water all-at-once
717 rather than in small incremental amounts. However, applying water all-at-once also pushes NO_3^-
718 deeper into the soil profile compared to applying water in increments, especially if wetter
719 antecedent moisture conditions exist. We conclude that ideal incremental AgMAR applications
720 and hydraulic loadings can be designed to promote denitrification within the root zone and
721 prevent N leaching to groundwater, but this treatment depends on the underlying stratigraphy and
722 site characteristics. Therefore, the site's underlying geology, initial soil moisture content, and

723 depth to the water table influences the water quality outcomes of implementing AgMAR. We
 724 recommend future studies to focus on the multiyear effects of AgMAR on N cycling, as well as
 725 management practices (i.e. cover cropping) that reduce residual N and increase labile DOC
 726 movement into the deep subsurface to increase available electron donors for denitrification.
 727

728 **Acknowledgements**

729 This material is based upon work supported as part of the DOE-SCGSR project, which is
 730 funded by the U.S. Department of Energy Biological and Environmental Science Priority
 731 Research Area, and as part of the Watershed Function Science Focus Area, which is funded by
 732 the U.S. Department of Energy, Office of Science, Office of Biological and Environmental
 733 Research, under Award Number DE-AC02-05CH11231 to Lawrence Berkeley National
 734 Laboratory. Partial support provided by Lawrence Berkeley Laboratory's Directed Research and
 735 Development Program. Additionally, this work was supported by a grant from the Almond
 736 Board of California. Data for determining how the data clustered can be found in Waterhouse et
 737 al. (in prep) and on the ESS-DIVE repository hosted by Lawrence Berkeley National Lab. The
 738 data gathered for this project would not be possible without the help of technicians, graduate and
 739 undergraduate students: Feifan Yang, Zaira Joaquin-Morales, and Rebecca Serata.
 740

741 **References**

742 1. Akhavan, M., Imhoff, P.T., Andres, A.S., Finsterle, S., 2013. Model evaluation of denitrification under
743 rapid infiltration basin systems. *J. Contam. Hydrol.* 152, 18–34.
744 <https://doi.org/10.1016/j.jconhyd.2013.05.007>

745 2. Arora, B., Mohanty, B.P., McGuire, J.T., Cozzarelli, I.M. 2013. Temporal dynamics of biogeochemical
746 processes at the Norman Landfill site. *Water Resources Research*, 49(10), pp.6909-6926.

747 3. Arora B., Sengör S.S., Steefel C.I. 2015. A reactive transport benchmark on heavy metal cycling in lake
748 sediments. *Comput. Geosci.* 19:613–633. doi:10.1007/s10596-014- 9445-8

749 4. Arora, B., Spycher, N.F., Steefel, C.I., Molins, S., Bill, M., Conrad, M.E., Dong, W., Faybishenko, B.,
750 Tokunaga, T.K., Wan, J., Williams, K.H., Yabusaki, S.B., 2016. Influence of hydrological, biogeochemical
751 and temperature transients on subsurface carbon fluxes in a flood plain environment. *Biogeochemistry* 127,
752 367–396. <https://doi.org/10.1007/s10533-016-0186-8>

753 5. Ascott, M.J., Gooddy, D.C., Wang, L., Stuart, M.E., Lewis, M.A., Ward, R.S., Binley, A.M., 2017. Global
754 patterns of nitrate storage in the vadose zone. *Nat. Commun.* 8, 1416. <https://doi.org/10.1038/s41467-017-01321-w>

755 6. Ascott, M.J., Wang, L., Stuart, M.E., Ward, R.S., Hart, A., 2016. Quantification of nitrate storage in the
756 vadose (unsaturated) zone: a missing component of terrestrial N budgets. *Hydrol. Process.* 30, 1903–1915.
757 <https://doi.org/10.1002/hyp.10748>

758 7. Bachand, P.A.M., Roy, S.B., Choperena, J., Cameron, D., Horwath, W.R., 2014. Implications of using on-
759 farm flood flow capture to recharge groundwater and mitigate flood risks along the Kings River, CA.
760 *Environ. Sci. Technol.* 48, 13601–13609. <https://doi.org/10.1021/es501115c>

761 8. Baram, S., Couvreur, V., Harter, T., Read, M., Brown, P.H., Kandelous, M., Smart, D.R., Hopmans, J.W.,
762 2016. Estimating Nitrate Leaching to Groundwater from Orchards: Comparing Crop Nitrogen Excess,
763 Deep Vadose Zone Data-Driven Estimates, and HYDRUS Modeling. *Vadose Zo. J.* 15, 0.
764 <https://doi.org/10.2136/vzj2016.07.0061>

765 9. Bonin, P., Gilewicz, M., Bertrand, J.C., 1989. Effects of oxygen on each step of denitrification on
766 *Pseudomonas nautica*. *Can. J. Microbiol.* 35, 1061–1064. <https://doi.org/10.1139/m89-177>

767 10. Brockman FJ, Kieft TL, Fredrickson JK, Bjornstad BN, Li SW, Spangenburg W, Long PE 1992.
768 Microbiology of vadose zone paleosols in south-central Washington State. *Microb Ecol* 23:279-301.

769 11. Botros, Farag E, Onsoy, Yuksel S, Ginn, Timothy R, Harter, T., 2012. Richards Equation - Based Modeling
770 to Estimate Flow and Nitrate Transport in a Deep Alluvial Vadose Zone. *Vadose Zo. J.* 11.
771 <https://doi.org/10.2136/vzj2011.0145>

772 12. Bundt, M., Widmer, F., Pesaro, M., Zeyer, J., Blaser, P., 2001. Preferential flow paths: Biological “hot
773 spots” in soils. *Soil Biol. Biochem.* 33, 729–738. [https://doi.org/10.1016/S0038-0717\(00\)00218-2](https://doi.org/10.1016/S0038-0717(00)00218-2)

774 13. Butterbach-Bahl, K., Baggs, E.M., Dannenmann, M., Kiese, R., Zechmeister-Boltenstern, S., 2013. Nitrous
775 oxide emissions from soils: how well do we understand the processes and their controls? *Philos. Trans. R.*
776 *Soc. Lond. B. Biol. Sci.* 368, 20130122. <https://doi.org/10.1098/rstb.2013.0122>

777 14. California Department of Food and Agriculture. Crop Report 2017.
778 <http://www.stanag.org/pdf/cropreport/cropreport2017.pdf>

779 15. Carlson, H.K., Clark, Iain C., Melnyk, R.A., Coates, J.D., 2012. Toward a mechanistic understanding of
780 anaerobic nitrate-dependent iron oxidation: Balancing electron uptake and detoxification. *Front. Microbiol.*
781 3, 1–6. <https://doi.org/10.3389/fmicb.2012.00057>

782 16. Chaopricha, N.T., Marín-spiotta, E., 2013. Soil burial contributes to deep soil organic carbon storage. *Soil*
783 *Biol. Biochem.* 69, 251–264.

784 17. Cressey, E.L., Dungait, J.A.J., Jones, D.L., Nicholas, A.P., Quine, T.A., 2018. Soil microbial populations in
785 deep floodplain soils are adapted to infrequent but regular carbon substrate addition. *Soil Biol. Biochem.*
786 122, 60–70. <https://doi.org/10.1016/j.soilbio.2018.04.001>

787 18. Doane, T.A., Horwath, W.R., 2003. Spectrophotometric Determination of Nitrate with a Single Reagent.
788 *Analytical Letters* 36, 2713–2722.

789 19. Doussan et al. 1997 River bank filtration: modelling of the changes in water chemistry with emphasis on
790 nitrogen species. *Journal of Contaminant Hydrology* 25 (1997) 129-156.

791 20. Dutta, T., Carles-Brangarí, A., Fernández-García, D., Rubol, S., Tirado-Conde, J., Sanchez-Vila, X., 2015.
792 Vadose zone oxygen (O₂) dynamics during drying and wetting cycles: An artificial recharge laboratory
793 experiment. *J. Hydrol.* 527, 151–159. <https://doi.org/10.1016/j.jhydrol.2015.04.048>

794

- 795 21. Dwivedi, D., Arora, B., Steefel, C.I., Dafflon, B., Versteeg, R. 2018. Hot spots and hot moments of
796 nitrogen in a riparian corridor. *Water Resources Research*, 54(1), pp.205-222.
- 797 22. Groffman, P.M., Holland, E.A., Myrold, D.D., Robertson, G.P., Zou, X. 1999. Denitrification. Pages 272-
798 288 in G.P. Robertson, D.C. Coleman, C.S. Bledsoe, P. Sollins (editors). *Standard soil methods for long-*
799 *term ecological research*. Oxford University Press, New York, NY, USA.
- 800 23. Handley KM, VerBerkmoes NC, Steefel CI et al (2013) Bios-
801 timation induces syntrophic interactions
802 that impact C, S and N cycling in a sediment microbial community. *ISME J* 7:800–816.
doi:10.1038/ismej.2012.148
- 803 24. Hanson, B.R., Šimůnek, J., Hopmans, J.W., 2006. Evaluation of urea-ammonium-nitrate fertigation with
804 drip irrigation using numerical modeling. *Agric. Water Manag.* 86 (1), 102–113.
- 805 25. Harden G.W., 1987. Soils Developed in Granitic Alluvium near Merced, California. U.S. GEOLOGICAL
806 SURVEY BULLETIN 1590-A
- 807 26. Harter, T., Onsoy, Y.S., Heeren, K., Denton, M., Weissmann, G., Hopmans, J.W., Horwath, W.R., 2008.
808 Deep vadose zone hydrology demonstrates fate of nitrate in eastern San Joaquin Valley. *Calif. Agric.* 59,
809 124–132. <https://doi.org/10.3733/ca.v059n02p124>
- 810 27. Hunter K.S., Wang Y., Van Cappellen P. 1998. Kinetic modeling of microbially-driven redox chemistry of
811 subsurface environments: coupling transport, microbial metabolism and geochemistry. *J. Hydrol.* 209:53–
812 80. doi:10.1016/S0022-1694(98)00157-7
- 813 28. Jardine, P.M., Mayes, M. a., Mulholland, P.J., Hanson, P.J., Tarver, J.R., Luxmoore, R.J., McCarthy, J.F.,
814 Wilson, G. V., 2006. Vadose Zone Flow and Transport of Dissolved Organic Carbon at Multiple Scales in
815 Humid Regimes. *Vadose Zo. J.* 5, 140. <https://doi.org/10.2136/vzj2005.0036>
- 816 29. Jahangir, M.M.R., Khalil, M.I., Johnston, P., Cardenas, L.M., Hatch, D.J., Butler, M., Barrett, M.,
817 O’flaherty, V., Richards, K.G., 2012. Denitrification potential in subsoils: A mechanism to reduce nitrate
818 leaching to groundwater. *Agric. Ecosyst. Environ.* 147, 13–23. <https://doi.org/10.1016/j.agee.2011.04.015>
- 819 30. Kirschbaum, M.U.F., 1995. The temperature dependence of soil organic matter decomposition, and the
820 effect of global warming on soil organic C storage. *Soil Biol. Biochem.* 27, 753–760.
821 [https://doi.org/10.1016/0038-0717\(94\)00242-S](https://doi.org/10.1016/0038-0717(94)00242-S)
- 822 31. Kocis, T.N., Dahlke, H.E., 2017. Availability of high-magnitude streamflow for groundwater banking in
823 the Central Valley, California. *Environ. Res. Lett.* 12. <https://doi.org/10.1088/1748-9326/aa7b1b>
- 824 32. Landon M.K., Belitz K. 2006, Ground-Water Quality Data in the Central Eastside San Joaquin Basin 2006:
825 Results from the California GAMA Program. USGS Data Series 325, In cooperation with the California
826 State Water Resources Control Board
- 827 33. Lovley, D.R., Phillips, E.J.P., 1987. Rapid assay for microbially reducible ferric iron in aquatic sediments.
828 *Appl. Environ. Microbiol.* 53, 1536–1540. <https://doi.org/10.1007/BF01611203>
- 829 34. Maggi et al. 2008 A mechanistic treatment of the dominant soil nitrogen cycling processes: Model
830 development, testing, and application. *JOURNAL OF GEOPHYSICAL RESEARCH*, VOL. 113, G02016,
831 doi:10.1029/2007JG000578, 2008
- 832 35. Marín-Spiotta, E., Chaopricha, N.T., Plante, A.F., Diefendorf, A.F., Mueller, C.W., Grandy, A.S., Mason,
833 J.A., 2014. Long-term stabilization of deep soil carbon by fire and burial during early Holocene climate
834 change. *Nat. Geosci.* 7, 428–432. <http://dx.doi.org/10.1038/ngeo2169>.
- 835 36. Mayer KU, Frind EO, Blowes DW (2002) Multicomponent reactive transport modeling in variably
836 saturated porous media using a generalized formulation for kinetically controlled reactions. *Water Resour*
837 *Res* 38:13–1–13–21. doi: 10.1029/2001WR000862
- 838 37. McCoy, E.L., Boast, C.W., Stehouwer, R.C., Klavivko, E.J., 1994. Macropore hydraulics: taking a
839 sledgehammer to classical theory. In: Lal, R., Stewart, B.A. (Eds.), *Soil Processes and Water Quality*.
840 Lewis Publishers, Boca Raton. p. 303-348.
- 841 38. Meyer, N., Meyer, H., Welp, G., Amelung, W., 2018. Soil respiration and its temperature sensitivity (Q10):
842 Rapid acquisition using mid-infrared spectroscopy. *Geoderma* 323, 31–40.
843 <https://doi.org/10.1016/j.geoderma.2018.02.031>
- 844 39. Morel FMM, Hering JG (1993) Principles and applications of aquatic chemistry. Wiley, New York
- 845 40. Neal, R.H., G. Sposito, K.M. Holtzclaw, and S.J. Traina. 1987. Selenite adsorption on alluvial soils: I. Soil
846 composition and pH effects. *Soil Sci. Soc. Am. J.* 51:1161-1165
- 847 41. Palmer K, Drake HL, Horn MA (2010) Association of novel and highly diverse acid-tolerant denitrifiers
848 with N2O fluxes of an acidic fen. *Appl Environ Microbiol* 76:1125–1134. doi:10.1128/AEM.02256-09

- 849 42. Phogat, V., Skewes, M.A., Cox, J.W., Sanderson, G., Alam, J., Simunek, J. "Seasonal simulation of water,
850 salinity and nitrate dynamics under drip irrigated mandarin (*Citrus reticulata*) and assessing management
851 options for drainage and nitrate leaching." *Journal of Hydrology* 513 (2014): 504-516.
- 852 43. Pratt, P.F., Jones, W., Hunsaker, V.E., 1972. Nitrate in Deep Soil Profiles in Relation to Fertilizer Rates
853 and Leaching Volume. *J. Environ. Qual.* 1, 97–102.
- 854 44. Pruess, K., Oldenburg, C., Moridis, G., 1999. TOUGH2 User's Guide, Version 2.0. Lawrence Berkeley
855 National Laboratory Report LBNL-43134.
- 856 45. Rodell, M., Famiglietti, J.S., Wiese, D.N., Reager, J.T., Beaudoin, H.K., Landerer, F.W., Lo, M.-H., 2018.
857 Emerging trends in global freshwater availability. *Nature* 1. <https://doi.org/10.1038/s41586-018-0123-1>
- 858 46. Salehi, A., Navabian, M., Varaki, M.E., Pirmoradian, N., 2017. Evaluation of HYDRUS-2D model to
859 simulate the loss of nitrate in subsurface controlled drainage in a physical model scale of paddy fields.
860 *Paddy Water Environ.* 15, 433–442. <https://doi.org/10.1007/s10333-016-0561-z>
- 861 47. Schaap, M.G., Leij, F.J., van Genuchten, M.T. 2001. Rosetta: a computer program for estimating soil
862 hydraulic parameters with hierarchical pedotransfer functions. *J. Hydrol.* 251, 163-176
- 863 48. Schmidt, C.M., Fisher, A.T., Racz, A.J., Lockwood, B.S., Huertos, M.L., 2011. Linking denitrification and
864 infiltration rates during managed groundwater recharge. *Environ. Sci. Technol.* 45, 9634–9640.
865 <https://doi.org/10.1021/es2023626>
- 866 49. Soil Survey Laboratory Methods Manual. 2004. Texture by Pipette Analysis. Soil Survey Investigations
867 Report No. 42. V. 4. p. 14-21.
- 868 50. Sonnenthal, Eric, Spycher, Nicolas, and USDOE. *TOUGHREACT (TREAT) v3.32*. Computer software.
869 USDOE. 28 Feb. 2014. Web. doi:10.11578/dc.20190130.1.
- 870 51. Stookey, L.L., 1970. Ferrozine-A New Spectrophotometric Reagent for Iron. *Anal. Chem.* 42, 779–781.
871 <https://doi.org/10.1021/ac60289a016>
- 872 52. Syswerda, S.P., Corbin, A.T., Mokma, D.L., Kravchenko, A.N., Robertson, G.P. 2011. Agricultural
873 management and soil carbon storage in surface versus deep layers. *Soil Sci. Soc. Amer. Journal.* 75: 92-
874 101.
- 875 53. Thomas, G., 1996. Soil pH and soil acidity. In: Sparks, D.L. (Ed.), *Methods of soil analysis. Part 3.*
876 *Chemical methods.* Soil Sci. Soc. Am.pp. 475–490 (Madison WI). Throckmorton,
- 877 54. van der Laan, M., Annandale, J.G., Bristow, K.L., Stürzaker, R.J., Du Preez, C.C., Thorburn, P.J., 2013.
878 Modelling nitrogen leaching: Are we getting the right answer for the right reason? *Agric. Water Manag.*
879 133, 74–80. <https://doi.org/10.1016/j.agwat.2013.10.017>
- 880 55. Van Meter, K.J., Basu, N.B., Veenstra, J.J. and Burras, C.L., 2016. The nitrogen legacy: emerging evidence
881 of nitrogen accumulation in anthropogenic landscapes. *Environmental Research Letters*, 11(3), p.035014.
- 882 56. Waterhouse H, Bachand S, Mountjoy D, Choperena J, Bachand P, Dahlke H, Horwath W. 2020.
883 Agricultural managed aquifer recharge — water quality factors to consider. *Calif Agr* 74(3):144-
884 154. <https://doi.org/10.3733/ca.2020a0020>.
- 885 57. Weissmann, G.S., Mount, J.F., and Fogg, G.E., 2002a, Glacially driven cycles in accumulation space and
886 sequence stratigraphy of a stream dominated alluvial fan, San Joaquin Valley, California, U.S.A.: *Journal*
887 *of Sedimentary Research*, v. 72, no. 2, p. 240–251.
- 888 58. Weissmann, G.S., Zhang, Y., LaBolle, E.M., and Fogg, G.E., 2002b, Dispersion of groundwater age in an
889 alluvial aquifer system: *Water Resources Research*, v. 38, p. 1198–1211, doi: 10.1029/2001WR000907.
- 890 59. White A.F., Blum A.E., Schulz M.S., Bullen T.D., Harden J.W., Peterson M.L., 1996. Chemical
891 weathering rates of a soil chronosequence on granitic alluvium: I. Quantification of mineralogical and
892 surface area changes and calculation of primary silicate reaction rates. *Geochimica et Cosmochimica Acta*,
893 Vol. 60, No. 14, pp. 2533-2550
- 894 60. Wu Y, Ajo-Franklin JB, Spycher N et al (2011) Geophysical monitoring and reactive transport modeling of
895 ureolyti- cally-driven calcium carbonate precipitation. *Geochem Trans* 12:7. doi:10.1186/1467-4866-12-7
- 896 61. Xu, T., Sonnenthal, E. L., Spycher, N., and Zheng, L. (2017), TOUGH- REACT—A simulation program
897 for non-isothermal multiphase reactive geochemical transport in variably saturated geologic media:
898 Applications to geothermal injectivity and CO2 geological sequestration, *Comput. Geosci.*, 32(2), 145–165.
- 899 62. Yabusaki, S.B., Wilkins, M.J., Fang, Y., Williams, K.H., Arora, B., Bargar, J., Beller, H.R., Bouskill,
900 N.J., Brodie, E.L., Christensen, J.N., Conrad, M.E., Danczak, R.E., King, E., Soltanian, M.R., Spycher,
901 N.F, Steefel, C.I., Tokunaga, T.K., Versteeg, R., Waichler, S.R., Wainwright, H.M. *Environmental Science*
902 *& Technology* 2017 51 (6), 3307-3317 DOI: 10.1021/acs.est.6b04873

903
904